

This work was written as part of one of the author's official duties as an Employee of the United States Government and is therefore a work of the United States Government. In accordance with 17 U.S.C. 105, no copyright protection is available for such works under U.S. Law. Access to this work was provided by the University of Maryland, Baltimore County (UMBC) ScholarWorks@UMBC digital repository on the Maryland Shared Open Access (MD-SOAR) platform.

Please provide feedback

Please support the ScholarWorks@UMBC repository by emailing [scholarworks-group@umbc.edu](mailto:scholarworks-group@umbc.edu) and telling us what having access to this work means to you and why it's important to you. Thank you.

## RESEARCH ARTICLE

10.1002/2016JD025067

## An observationally constrained evaluation of the oxidative capacity in the tropical western Pacific troposphere

## Key Points:

- Observations from the CONTRAST campaign in the tropical western Pacific are used to infer the concentration of tropospheric OH
- The empirically based value of tropospheric column OH is 0 to 20% larger than found within global models
- Underestimations of observed  $\text{NO}_x$ ,  $\text{CH}_3\text{CHO}$ , and HCHO drive most differences between column OH within global models and empirically based value

## Supporting Information:

- Figures S1–S14

## Correspondence to:

J. M. Nicely,  
julie.m.nicely@nasa.gov

## Citation:

Nicely, J. M., et al. (2016), An observationally constrained evaluation of the oxidative capacity in the tropical western Pacific troposphere, *J. Geophys. Res. Atmos.*, 121, 7461–7488, doi:10.1002/2016JD025067.

Received 9 MAR 2016

Accepted 1 JUN 2016

Accepted article online 5 JUN 2016

Published online 24 JUN 2016

Julie M. Nicely<sup>1,2</sup>, Daniel C. Anderson<sup>3</sup>, Timothy P. Canty<sup>3</sup>, Ross J. Salawitch<sup>1,3,4</sup>, Glenn M. Wolfe<sup>5,6</sup>, Eric C. Apel<sup>7</sup>, Steve R. Arnold<sup>8</sup>, Elliot L. Atlas<sup>9</sup>, Nicola J. Blake<sup>10</sup>, James F. Bresch<sup>7</sup>, Teresa L. Campos<sup>7</sup>, Russell R. Dickerson<sup>3</sup>, Bryan Duncan<sup>5</sup>, Louisa K. Emmons<sup>7</sup>, Mathew J. Evans<sup>11,12</sup>, Rafael P. Fernandez<sup>13,14</sup>, Johannes Flemming<sup>15</sup>, Samuel R. Hall<sup>7</sup>, Thomas F. Hanisco<sup>5</sup>, Shawn B. Honomichi<sup>7</sup>, Rebecca S. Hornbrook<sup>7</sup>, Vincent Huijnen<sup>16</sup>, Lisa Kaser<sup>7</sup>, Douglas E. Kinnison<sup>7</sup>, Jean-Francois Lamarque<sup>7</sup>, Jingqiu Mao<sup>17,18</sup>, Sarah A. Monks<sup>8,19,20</sup>, Denise D. Montzka<sup>7</sup>, Laura L. Pan<sup>7</sup>, Daniel D. Riemer<sup>9</sup>, Alfonso Saiz-Lopez<sup>13</sup>, Stephen D. Steenrod<sup>5,21</sup>, Meghan H. Stell<sup>7,22</sup>, Simone Tilmes<sup>7</sup>, Solene Turquety<sup>23</sup>, Kirk Ullmann<sup>7</sup>, and Andrew J. Weinheimer<sup>7</sup>

<sup>1</sup>Department of Chemistry and Biochemistry, University of Maryland, College Park, Maryland, USA, <sup>2</sup>Now at Atmospheric Chemistry and Dynamics Laboratory, NASA Goddard Space Flight Center, Greenbelt, Maryland, USA, <sup>3</sup>Department of Atmospheric and Oceanic Science, University of Maryland, College Park, Maryland, USA, <sup>4</sup>Earth System Science Interdisciplinary Center, University of Maryland, College Park, Maryland, USA, <sup>5</sup>Atmospheric Chemistry and Dynamics Laboratory, NASA Goddard Space Flight Center, Greenbelt, Maryland, USA, <sup>6</sup>Joint Center for Earth Systems Technology, University of Maryland, Baltimore County, Baltimore, Maryland, USA, <sup>7</sup>National Center for Atmospheric Research, Boulder, Colorado, USA, <sup>8</sup>Institute for Climate and Atmospheric Science, University of Leeds, Leeds, UK, <sup>9</sup>Department of Atmospheric Sciences, Rosenstiel School of Marine and Atmospheric Science, University of Miami, Miami, Florida, USA, <sup>10</sup>Department of Chemistry, University of California, Irvine, California, USA, <sup>11</sup>National Centre for Atmospheric Science, University of York, York, UK, <sup>12</sup>Department of Chemistry, University of York, York, UK, <sup>13</sup>Department of Atmospheric Chemistry and Climate, Institute of Physical Chemistry Rocasolano, CSIC, Madrid, Spain, <sup>14</sup>National Research Council (CONICET), Mendoza, Argentina, <sup>15</sup>European Centre for Medium-Range Weather Forecasts, Reading, UK, <sup>16</sup>Royal Netherlands Meteorological Institute, De Bilt, Netherlands, <sup>17</sup>Program in Atmospheric and Oceanic Sciences, Princeton University, Princeton, New Jersey, USA, <sup>18</sup>Geophysical Fluid Dynamics Laboratory/National Oceanic and Atmospheric Administration, Princeton, New Jersey, USA, <sup>19</sup>Now at Chemical Sciences Division, Earth System Research Laboratory, National Oceanic and Atmospheric Administration, Boulder, Colorado, USA, <sup>20</sup>Now at Cooperative Institute for Research in Environmental Sciences, University of Colorado Boulder, Boulder, Colorado, USA, <sup>21</sup>Universities Space Research Association, Columbia, Maryland, USA, <sup>22</sup>Metropolitan State University of Denver, Denver, Colorado, USA, <sup>23</sup>Laboratoire de Météorologie Dynamique, IPSL, Sorbonne Universités, UPMC Univ Paris 06, Paris, France

**Abstract** Hydroxyl radical (OH) is the main daytime oxidant in the troposphere and determines the atmospheric lifetimes of many compounds. We use aircraft measurements of  $\text{O}_3$ ,  $\text{H}_2\text{O}$ , NO, and other species from the Convective Transport of Active Species in the Tropics (CONTRAST) field campaign, which occurred in the tropical western Pacific (TWP) during January–February 2014, to constrain a photochemical box model and estimate concentrations of OH throughout the troposphere. We find that tropospheric column OH ( $\text{OH}^{\text{COL}}$ ) inferred from CONTRAST observations is 12 to 40% higher than found in chemical transport models (CTMs), including CAM-chem-SD run with 2014 meteorology as well as eight models that participated in POLMIP (2008 meteorology). Part of this discrepancy is due to a clear-sky sampling bias that affects CONTRAST observations; accounting for this bias and also for a small difference in chemical mechanism results in our empirically based value of  $\text{OH}^{\text{COL}}$  being 0 to 20% larger than found within global models. While these global models simulate observed  $\text{O}_3$  reasonably well, they underestimate  $\text{NO}_x$  ( $\text{NO} + \text{NO}_2$ ) by a factor of 2, resulting in  $\text{OH}^{\text{COL}}$  ~30% lower than box model simulations constrained by observed NO. Underestimations by CTMs of observed  $\text{CH}_3\text{CHO}$  throughout the troposphere and of HCHO in the upper troposphere further contribute to differences between our constrained estimates of OH and those calculated by CTMs. Finally, our calculations do not support the prior suggestion of the existence of a tropospheric OH minimum in the TWP, because during January–February 2014 observed levels of  $\text{O}_3$  and NO were considerably larger than previously reported values in the TWP.

## 1. Introduction

The hydroxyl radical (OH) is the most important oxidant in the troposphere. Abundances of many species, such as  $\text{CH}_4$ , CO,  $\text{SO}_2$ , and certain halocarbons, are determined in part by the concentration of tropospheric OH. The lifetime of methane ( $\text{CH}_4$ ), the second most important anthropogenic greenhouse gas, is primarily

controlled by tropospheric OH [Levy, 1971; Prather et al., 2012]. The geographic distribution of carbon monoxide (CO), a long-lived anthropogenic pollutant, in global chemistry models depends on the accuracy of tropospheric OH as well as CO emissions [Levy, 1971; Shindell et al., 2006; Monks et al., 2015; Strode et al., 2015]. The lifetime of SO<sub>2</sub>, a product of anthropogenic activities, is also sensitive to the concentration of OH [Calvert et al., 1978]. Of the very short lived (VSL) halocarbons, dibromomethane (CH<sub>2</sub>Br<sub>2</sub>), bromochloromethane (CH<sub>2</sub>BrCl), and all chlorocarbons (CH<sub>2</sub>Cl<sub>2</sub>, CHCl<sub>3</sub>, and higher-order compounds) are lost predominantly by reaction with OH [Stratospheric Processes and their Role in Climate (SPARC), 2013]. Finally, the OH-initiated oxidation of volatile organic compounds (VOCs) is an important production mechanism for tropospheric ozone (O<sub>3</sub>) [Hough and Derwent, 1987].

A primary motivation for improved understanding of tropical tropospheric OH arises from the considerable range in the global burden of OH that is estimated in global models. Concentrations of OH maximize near the surface in the tropical troposphere [Spivakovsky et al., 2000], so the mean tropospheric abundance of OH and CH<sub>4</sub> lifetime within global models are largely influenced by the tropics [Bloss et al., 2005]. The Atmospheric Chemistry and Climate Model Intercomparison Project (ACCMIP) analyzed 14 models and found a 62% spread (full range of values divided by the multimodel mean) in global burdens of OH [Voulgarakis et al., 2013]. Most of the models analyzed were chemistry-climate models (CCMs); i.e., they were run using internally generated dynamics and atmospheric moisture. Other projects that compare output solely from chemistry transport models (CTMs, in which model dynamics are based upon meteorological reanalysis fields) might be expected to have better constrained OH due to the use of similar transport. Our analysis of one such project, the POLARCAT Model Intercomparison Project (POLMIP) [Emmons et al., 2015], suggests that the spread in global mean OH across eight models is ~31%: a smaller range, but for fewer models (J. M. Nicely et al., manuscript in preparation). For POLMIP, effort was made to use the same emissions of NO<sub>x</sub>, CO, and VOCs among the various models, which also likely explains the smaller range of OH in this CTM comparison. Other intercomparison studies show large variations in computed OH: Shindell et al. [2006] reported a 65% spread in global mean OH among 26 models, and Fiore et al. [2009] found an 80% spread among 12 models. Both of these studies examined OH from global models run as CTMs. Furthermore, there is considerable spread in the computed difference in tropospheric mean OH between preindustrial and present, ranging from a 14% increase to a 14% decrease, among 16 global models examined by Naik et al. [2013].

Considering these large spreads in OH burdens among various global models, it is not surprising that models also disagree on the future evolution of OH concentrations. Voulgarakis et al. [2013] found that the ACCMIP models do not agree on the sign of change in the global burden of OH over the next century. Early estimates of the effect of climate change on atmospheric chemistry predicted that global OH burdens would decline with expected increases in global burdens of CH<sub>4</sub> and CO [e.g., Houghton et al., 1996]. However, many facets of OH chemistry were simplified in these studies. It is now believed that other factors, including increasing water vapor and NO<sub>x</sub> [Stevenson et al., 2000; Hauglustaine et al., 2005] as well as rising temperatures leading to faster CH<sub>4</sub> oxidation [Johnson et al., 1999], could instead result in larger future burdens of OH [Stevenson et al., 2006]. Given that climate modelers seek to understand a wide range of possible future conditions through consideration of many factors, the community should define how well various models represent OH in the contemporary atmosphere as a first step to assessing the reliability of projections of tropospheric OH.

Another issue confronting the modeling community is that global models [Naik et al., 2013] systematically underestimate  $\tau_{\text{CH}_4}$  by ~1.75 years (~16%) relative to the current empirical best estimate of 11.2 years [Prather et al., 2012; Intergovernmental Panel on Climate Change, 2013]. Here and throughout, we use  $\tau_{\text{CH}_4}$  to refer to the photochemical lifetime of CH<sub>4</sub> with respect to loss by tropospheric OH. Measurements of methyl chloroform (MCF: CH<sub>3</sub>CCl<sub>3</sub>) decay rates are most commonly used to empirically determine the mean tropospheric concentration of OH as well as  $\tau_{\text{CH}_4}$  [Singh, 1977; Prinn et al., 2005; Montzka et al., 2011]. For example, Prinn et al. [2005] reported  $\tau_{\text{CH}_4}$  of  $10.2^{+0.9}_{-0.7}$  years in 2003 based on the observed decay of MCF. More recently, Prather et al. [2012] reported a value for  $\tau_{\text{CH}_4}$  of  $11.2 \pm 1.3$  years (uncertainty is one standard deviation ( $\sigma$ ) confidence interval). The Prather et al. [2012] analysis also included loss of CH<sub>4</sub> by soils, reactions in the stratosphere, reaction with tropospheric atomic chlorine, as well as the reaction with tropospheric OH, leading to an overall lifetime of  $9.1 \pm 0.9$  years. The burdens of tropospheric OH from the ACCMIP CCMs and POLMIP CTMs discussed earlier yield mean CH<sub>4</sub> lifetimes of  $9.8 \pm 1.6$  [Voulgarakis et al., 2013] and  $8.1 \pm 0.9$  years (J. M. Nicely et al., manuscript in preparation), respectively, where the uncertainties are  $1\sigma$  about the multimodel

mean. The discrepancy between MCF-based and model-based estimates of  $\tau_{\text{CH}_4}$  could be resolved if the burden of tropospheric OH within global models were shown to be too high, based on actual tropospheric abundances. Another possible resolution to this discrepancy would be an error in the MCF-based estimate of  $\tau_{\text{CH}_4}$ . *Krol and Lelieveld* [2003] pointed out that stockpiling and later release of MCF, as the Montreal Protocol was being implemented, could lead to an uncertainty that during the time of release of stockpiled MCF, if not considered, would lead to an overestimate of  $\tau_{\text{CH}_4}$  via the MCF method and therefore could help resolve this discrepancy. *Wennberg et al.* [2004] noted the importance of air-sea exchange of MCF, which during times of oceanic release would similarly lead to an overestimate of  $\tau_{\text{CH}_4}$  by the MCF method. Conversely, *Wang et al.* [2008] used three-dimensional model estimates of OH, together with MCF abundance and emission data, to suggest the actual value of  $\tau_{\text{CH}_4}$  via the MCF method is longer than found in other studies.

The short-lived, reactive nature of OH as well as its low mixing ratio (a fraction of a part per trillion by volume, hereafter ppt) make OH a challenging compound to measure accurately. As a result, observational constraints on OH are often restricted in spatial and temporal coverage. In regions where air is convectively lofted to the tropopause, such as the tropical western Pacific (TWP) [*Newell and Gould-Stewart*, 1981; *Hatsushika and Yamazaki*, 2003; *Fueglistaler et al.*, 2004], quantification of the abundance of OH is crucial to evaluating the composition of air at the base of the stratosphere [*SPARC*, 2013]. Measurements of OH in the TWP are limited to several campaigns, including the Pacific Exploratory Mission-Tropics B (PEM-Tropics B) [*Tan et al.*, 2001], which sampled the upper troposphere over the Pacific in March–April 1999 but only skirted the warm pool region. Measurements of OH precursors from the accompanying PEM-Tropics A campaign in September–October 1996 were also used to calculate OH using a box model [*Olson et al.*, 2001]. The sampling from both PEM-Tropics campaigns is representative of the pristine Southern Hemisphere Pacific and relatively clean central Northern Hemisphere Pacific. Diurnally averaged OH concentrations from PEM-Tropics A and B maximize in the tropical lower troposphere, peaking at a value of  $\sim 1.7 \times 10^6 \text{ cm}^{-3}$  [*Olson et al.*, 2001]. This peak value of OH is similar to what we infer over the TWP warm pool. Similarly, the Mauna Loa Observatory Photochemistry Experiment (MLOPEX 2) found that observations of free tropospheric OH in the central Pacific at 10:00 A.M. during spring 1992 were  $\sim 4 \times 10^6 \text{ cm}^{-3}$  [*Eisele et al.*, 1996], similar to values calculated in our study. The Transport and Chemical Evolution over the Pacific (TRACE-P) campaign conducted measurements of OH across the Pacific Ocean [*Jacob et al.*, 2003], though the only results noted for the remote marine environment occurred at night [*Mauldin et al.*, 2003]. The STRAT campaign also provided observations of TWP OH when it sampled an upper tropospheric air parcel under sunlit conditions near Hawaii that had originated from convective outflow in the TWP. This air parcel had extremely low hydroxyl concentrations ( $\sim 0.5 \times 10^6 \text{ cm}^{-3}$ ), which *Gao et al.* [2014] suggested could be indicative of the TWP warm pool; the low number density of nitric oxide (i.e.,  $[\text{NO}] < 1 \times 10^8 \text{ cm}^{-3}$ ) suppressed the normally rapid conversion of  $\text{HO}_2$  to OH.

*Rex et al.* [2014] similarly found observational evidence of a marked OH minimum throughout the TWP troposphere. In this case, the OH minimum was driven by low mixing ratios of  $\text{O}_3$  ( $< 15$  ppb) measured by sondes during the TransBrom ship-based campaign in October 2009 [*Kruger and Quack*, 2013]. Calculations conducted using the GEOS-Chem model, which agreed well with the low  $\text{O}_3$  measurements [*Ridder et al.*, 2012], resulted in low values of  $[\text{OH}] (\leq 0.75 \times 10^6 \text{ cm}^{-3})$  likely as a result of suppressed primary production [*Rex et al.*, 2014]. While there are no direct measurements of OH in the central region of the TWP, the suggestion of the existence of depressed OH as a result of low concentrations of NO or  $\text{O}_3$  (or a combination of these two factors), which *Rex et al.* [2014] termed an “OH hole,” motivates the need for increased observational constraints to better quantify OH in the TWP.

The PEM-West A and B campaigns also provided measurements of many species with the exception of OH in the TWP region for boreal autumn 1991 and spring 1994, respectively [*Hoell et al.*, 1996, 1997]. Notably, during the springtime campaign, bimodal distributions of  $\text{NO}_x$  and  $\text{O}_3$  were observed frequently [*Crawford et al.*, 1997], consistent with observations from the Convective Transport of Active Species in the Tropics (CONTRAST) campaign [*Pan et al.*, 2015; *Anderson et al.*, 2016]. However, the PEM-West B observations differ from CONTRAST observations in that elevated CO did not accompany the high  $\text{NO}_x$  and  $\text{O}_3$  measurements. As a result, *Crawford et al.* [1997] attribute the elevated  $\text{NO}_x$  primarily to lightning occurring in conjunction with continental deep convection. *Anderson et al.* [2016] find high correlation of elevated  $\text{O}_3$  with elevated tracers of biomass burning, so the higher values of  $\text{NO}_x$  presented here are likely the result of burning activities over Africa and Southeast Asia in addition to lightning  $\text{NO}_x$  generation. Data from the PEM-West A campaign in

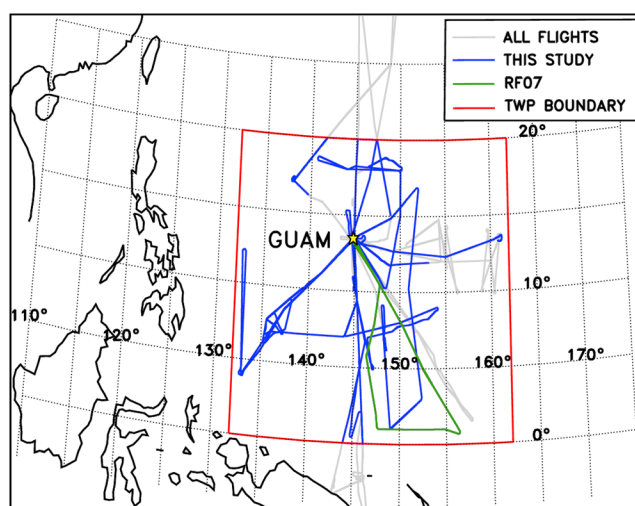


**Figure 1.** Flight tracks of the GV aircraft during the CONTRAST campaign, January–February 2014. Portions of flight tracks used in this study are shown in blue; criteria for including aircraft data are  $\text{SZA} \leq 60^\circ$ , latitude between  $0^\circ\text{N}$  and  $20^\circ\text{N}$ , and longitude between  $132^\circ\text{E}$  and  $162^\circ\text{E}$  (latitude/longitude bounds indicated by red box), and presence of valid data for  $\text{O}_3$  and  $\text{CO}$  at the time and location of observation. Portions of flight tracks not included in this study are shown in grey. Research Flight (RF) 07 is highlighted in green.

autumn, however, showed primarily clean conditions corresponding to the low  $\text{O}_3$ , low  $\text{NO}_x$  regime that was sometimes present in the springtime campaign [Crawford *et al.*, 1997].

Very short lived (VSL) halocarbons can contribute to  $\text{O}_3$  loss in the lowermost stratosphere [Salawitch *et al.*, 2005], a process facilitated by convective lofting in the TWP [Aschmann *et al.*, 2009; Ashfold *et al.*, 2012; Hossaini *et al.*, 2012; Fernandez *et al.*, 2014; Liang *et al.*, 2014]. We use the common convention that VSL refers to any species with a tropospheric lifetime of 6 months or less, such that the distribution within the troposphere is expected to be nonuniform [Law *et al.*, 2007]. With lifetimes on the order of days to months, the efficiency of these species passing into the stratosphere hinges on the concentration of OH in the TWP [Rex *et al.*, 2014].

We use data collected during the CONTRAST aircraft campaign [Pan *et al.*, 2016], conducted during January and February 2014 from Guam ( $13.5^\circ\text{N}$ ,  $144.8^\circ\text{E}$ ), to model the abundance of OH in the TWP. While OH was not observed during CONTRAST, a multitude of chemical species, radiative variables, and meteorological parameters needed to model the in situ production and loss of OH were measured. The DSMACC box model [Emmerson and Evans, 2009], constrained to observations of OH precursors and related species, is used to calculate instantaneous and 24 h average OH. We then compare our results to values of OH computed by the CAM-chem-SD model, run in the specified dynamics mode for 2014 [Lamarque *et al.*, 2012; Tilmes *et al.*, 2015]. Additional box model runs were performed to determine which OH precursor species drive the differences between the modeled and observationally derived OH. We also assess the impact on OH of high- $\text{O}_3$ , low- $\text{H}_2\text{O}$  (HOLW) structures frequently observed in the midtroposphere throughout CONTRAST [Pan *et al.*, 2015; Anderson *et al.*, 2016]. Additionally, the local lifetime of  $\text{CH}_2\text{Br}_2$  ( $\tau_{\text{CH}_2\text{Br}_2}$ ), a brominated VSL lost primarily by reaction with OH, is evaluated and compared to previously published estimates. Finally, we compare our observationally constrained OH distribution to output from the POLMIP CTMs to highlight a few possible shortcomings in these global models.

## 2. Data and Methods

### 2.1. CONTRAST Campaign

The CONTRAST campaign [Pan *et al.*, 2016] was based in Guam ( $13.5^\circ\text{N}$ ,  $144.8^\circ\text{E}$ ) during January and February 2014. Observations were obtained by a suite of chemical, meteorological, microphysical, and radiative instruments on board the NSF/NCAR Gulfstream V (GV) aircraft. The foci of various research flights (RFs) consisted of surveying the TWP, sampling convective outflow, and obtaining observations across both the Intertropical Convergence Zone and the subtropical jet stream. Our study uses observations acquired over the portion of the TWP sampled extensively during CONTRAST; i.e., the region bounded by latitudes  $0^\circ\text{N}$  to  $20^\circ\text{N}$ , longitudes  $132^\circ\text{E}$  to  $162^\circ\text{E}$  (Figure 1). We further restrict our study to data collected during times when measurements of  $\text{O}_3$  and  $\text{CO}$  exist and solar zenith angle ( $\text{SZA}$ )  $< 60^\circ$  (i.e., midday or higher solar illumination). Within these constraints, we analyzed data collected during the portions of RFs 04 to 15 that lie within the red box of Figure 1. Data collected during the three transit flights (RF 01, 02, and 16) are excluded, as are data collected during RF03 since measurements of  $\text{CO}$  are not available.

The CONTRAST measurements used in this study include O<sub>3</sub> and NO obtained on board the GV aircraft by chemiluminescence at a frequency of 1 Hz with 1σ precisions of 0.5 ppb and 10 ppt, respectively, both with uncertainties of 5% [Ridley and Grahek, 1990]. CO measurements were obtained using an Aero-Laser 5002 vacuum ultraviolet fluorescence instrument at a frequency of 1 Hz and with a 2σ uncertainty of 3 ppb ± 3% [Gerbig et al., 1999]. Water vapor mixing ratios were measured by an open-path laser hygrometer at a frequency of 1 Hz and 2σ precision of < 3% [Zondlo et al., 2010]. CH<sub>4</sub> measurements were made using a Picarro G2311-fm CO<sub>2</sub>/CH<sub>4</sub>/H<sub>2</sub>O cavity ringdown spectrometer with output provided at 1 Hz with a 1σ precision of 3 ppb [Crosson, 2008]. Formaldehyde (HCHO) was measured via laser-induced fluorescence by the NASA in situ airborne formaldehyde (ISAF) instrument with reported values at 1 Hz frequency and 2σ uncertainty of ± 20 ppt [Cazorla et al., 2015]. A number of organic trace gas measurements are used from the Trace Organic Gas Analyzer (TOGA) gas chromatograph/mass spectrometer (GCMS) instrument [Apel et al., 2015]. Acetone (CH<sub>3</sub>COCH<sub>3</sub>), isoprene (C<sub>5</sub>H<sub>8</sub>), propane (C<sub>3</sub>H<sub>8</sub>), methanol (CH<sub>3</sub>OH), and acetaldehyde (CH<sub>3</sub>CHO) were measured with a sampling time of 35 s and output every 2 min. Additionally, HCHO from TOGA is sporadically used when data from ISAF are unavailable. Limits of detection (uncertainties) for the TOGA species are the following: 20 ppt (20% or 40 ppt) for CH<sub>3</sub>COCH<sub>3</sub>, 1 ppt (15% or 2 ppt) for C<sub>5</sub>H<sub>8</sub>, 10 ppt (30% or 20 ppt) for C<sub>3</sub>H<sub>8</sub>, 20 ppt (30% or 40 ppt) for CH<sub>3</sub>OH, 5 ppt (20% or 10 ppt) for CH<sub>3</sub>CHO, and 20 ppt (100% or 80 ppt) for HCHO. Finally, photolysis frequencies for the reactions



are provided every 6 s, calculated from measurements of upwelling and downwelling, spectrally resolved actinic flux density by the HIAPER Airborne Radiation Package (HARP) [Shetter and Muller, 1999]. Total 1σ uncertainties for the photolysis frequencies of (R1) (hereafter denoted  $J(O^1D)$ ) and (R2) (denoted  $J(NO_2)$ ) are estimated to be 25% and 12%, respectively. These estimates account for calibration, instrumental, and spectral (including cross section and quantum yield) uncertainties.

The data set described above was adapted to a variable time resolution for this study because we conduct numerous box model simulations of observations collected along each flight track. For level altitude flight legs a resolution of 10 min is used, whereas a finer resolution of 30 s is implemented for aircraft ascent or descent. This variable time resolution preserves fine-scale features, such as HOLW structures, often observed within vertical profiles. Measurements are averaged (i.e., along either 30 s or 10 min intervals) when valid data are present. This choice of variable temporal resolution results in 2600 samples of atmospheric composition across the 12 flights.

## 2.2. DSMACC Box Model

We use the Dynamically Simple Model for Atmospheric Chemical Complexity (DSMACC) to perform box model calculations of OH [Emmerson and Evans, 2009]. This box model uses the Kinetic PreProcessor (KPP) [Damian et al., 2002], the Tropospheric Ultraviolet and Visible radiation model version 4.2 (TUV) [Palancar et al., 2011], and a subset (644 species; 2046 chemical reactions) of the Master Chemical Mechanism (MCM) [Jenkin et al., 1997; Saunders et al., 2003] version 3.3 [Jenkin et al., 2015]. The box model is constrained to CONTRAST measurements of meteorological variables, O<sub>3</sub>, CO, NO, HCHO, H<sub>2</sub>O, C<sub>3</sub>H<sub>8</sub>, CH<sub>4</sub>, C<sub>5</sub>H<sub>8</sub>, CH<sub>3</sub>COCH<sub>3</sub>, CH<sub>3</sub>OH, and CH<sub>3</sub>CHO mixing ratios, as well as  $J(O^1D)$  and  $J(NO_2)$ . Constraints for all nonradical chemical species (all chemicals listed above except NO) result in that variable being held fixed at the initial value for the duration of the model run. A box model simulation progresses through several solar cycles until diel steady state is achieved (i.e., the fractional change in concentrations of radical species from one solar cycle to the next is near zero). The sum of NO + NO<sub>2</sub> + NO<sub>3</sub> + N<sub>2</sub>O<sub>5</sub> + HO<sub>2</sub>NO<sub>2</sub> + HONO is held constant throughout a simulated solar cycle, but the concentrations of the individual species vary with solar illumination. At the end of each solar cycle, each of the NO<sub>y</sub> compounds listed above is scaled by the ratio of observed NO to modeled NO. This ensures that the total of the NO<sub>y</sub> species in the model is internally self-consistent with the observed NO concentrations. Photolysis frequencies also vary diurnally. They are first calculated by the TUV module for the latitude, longitude, and pressure coordinates of the specific observation and for albedo (0.05) and overhead column O<sub>3</sub> (224 Dobson units (DU) total column, 194 DU stratospheric column) values representative of the TWP for January/February. The photolysis frequencies are then scaled to the observed  $J$  value at the time of observation via a multiplicative factor. This multiplicative factor is applied throughout the diurnal cycles simulated by the model. The  $J$  values for other species are scaled according to a combination of the  $J(NO_2)$  and  $J(O^1D)$  scaling

factors, determined by the wavelength range in which the species photolyze. The calculated  $J$  values are insensitive to the chosen albedo and overhead column  $O_3$  values chosen above due to subsequent scaling of the  $J$  values to match the observations. Upon reaching diurnal steady state, the box model outputs the final 24 h (at 10 min intervals) of chemical concentrations,  $J$  values, and reaction rates, enabling us to evaluate both instantaneous OH (at the time of observation) and 24 h average OH.

For the analysis of OH during the CONTRAST campaign the box model is constrained to the 11 chemical measurements (noted above) obtained by instruments on board the GV aircraft, plus  $J(O^1D)$ ,  $J(NO_2)$ , temperature, pressure, latitude, longitude, and local solar time. These calculated OH values will hereafter be referred to as "GV OH." Additional box modeling calculations are performed, constrained to the output from the global models described below.

Given the variable temporal resolution of specific instruments, as well as occasional gaps due to instrument performance or routine calibrations, valid data are frequently unavailable. For example, only 311 of the aforementioned 2600 samples of atmospheric composition have valid measurements of all 13 GV parameters. To obtain a robust estimate of GV OH (i.e., representative of the mean state of the TWP during January and February 2014), we have developed a method to fill in missing data values. Given the importance and atmospheric variability of  $O_3$ , all atmospheric samples used here must include a valid measurement of  $O_3$ . For other species as well as  $J(O^1D)$  and  $J(NO_2)$ , if missing data occur before measurements of a particular variable have been made (i.e., during the initial leg) or after an instrument has stopped sampling, missing data are filled in by averaging all other valid measurements that exist within  $0.5^\circ$  latitude,  $0.5^\circ$  longitude, and 2000 m altitude for the specific flight. This helps ensure that the substitute value is from a similar air mass sampled close in location to where missing data are reported. For missing data that occur when measurements exist both earlier and later in the current flight, a value is found by linearly interpolating between the two closest valid data points. An exception is made for  $H_2O$  when altitude is varying; in these cases, gaps in the  $H_2O$  mixing ratio are either filled using the latitude/longitude/altitude binning method (if available) or the sampling interval is excluded from the analysis. For HCHO, we use measurements from the ISAF instrument whenever valid data points exist. When HCHO from ISAF is unavailable, observations from the TOGA instrument are used. In this case, regression of ISAF against TOGA HCHO is used on a flight-by-flight basis to account for instrument differences. The effect of this method for filling in missing data on our results is further examined in section 3.2.

Because the GV aircraft was sampling in the remote TWP, the mixing ratios of the organic trace gases measured by TOGA used in this analysis ( $C_3H_8$ ,  $C_5H_8$ ,  $CH_3COCH_3$ ,  $CH_3OH$ , and  $CH_3CHO$ ) were at times below the limit of detection (LOD) of the instrument. When the abundance of a compound was below the LOD, we specified abundance based on the number of "below LOD" data points reported in succession. Mixing ratio equal to 50% of the LOD was specified when fewer than 10 below LOD data points occurred in succession; conversely, a mixing ratio equal to 20% of the LOD was used when 10 or more below LOD data points occurred in succession. Isoprene ( $C_5H_8$ ) is the species most commonly affected by the TOGA LOD. Our scientific results are unaffected by any reasonable assumption for  $[C_5H_8]$  and the other organics when below the TOGA LOD, including specification of  $[C_5H_8] = 0$  within the model.

We have tagged each of the 13 GV variables, to assess for all 2600 samples whether and how data gaps were filled. The scientific results shown below are the same whether the analysis is based on the 300 sampling intervals when valid data exist for all species or the 2600 intervals considered below. We have chosen to show results for the 2600 intervals, since this provides more complete sampling of the TWP.

### 2.3. CAM-chem-SD (Winter 2014)

The Community Atmosphere Model version 4.0 (CAM4) is the atmospheric component of the global chemistry-climate Community Earth System Model (CESM) [Lamarque *et al.*, 2012; Tilmes *et al.*, 2015]. The model can be run with active chemistry, a configuration referred to as CAM-chem. For the winter 2014 calculations conducted for the CONTRAST campaign, the internally derived meteorological fields were nudged using NASA GEOS5 analysis fields [Tilmes *et al.*, 2015] with a horizontal resolution of  $0.94^\circ$  latitude  $\times$   $1.25^\circ$  longitude and 56 vertical levels, which we denote CAM-chem-SD (SD for specified dynamics). The model chemistry scheme includes a detailed representation of tropospheric and stratospheric chemistry ( $\sim 180$  species and  $\sim 500$  chemical reactions), including brominated [Fernandez *et al.*, 2014] and iodinated [Saiz-Lopez *et al.*, 2014] very short lived organic compounds. Anthropogenic emissions of  $O_3$  and aerosol precursors are from

RCP 6.0 for year 2014 [Meinshausen *et al.*, 2011; van Vuuren *et al.*, 2011], and biomass burning emissions are from the Fire Inventory for NCAR (FINN) [Wiedinmyer *et al.*, 2011].

Output from CAM-chem-SD includes all the species and variables used to constrain and initialize the box model, as described in section 2.2. The model output is linearly interpolated to the aircraft latitude, longitude, and local solar time for all flights in the campaign, providing us with “curtains,” or output at all model vertical levels along the space/time coordinate of each research flight. The curtain file model output allows for quantitative comparison of GV OH to CAM-chem-SD OH, for GV OH to be visualized in the context of surrounding atmospheric features, and for the causes of differences between GV OH and CAM-chem-SD OH to be assessed.

Variations between observationally constrained box model OH and global model OH may result from a number of factors, including differences in the chemical mechanism within the two models. The importance of the chemical mechanism is assessed by examining whether the box model can reproduce CAM-chem-SD OH, when constrained to the 13 precursor species output from CAM-chem-SD. We therefore perform box model calculations of OH based on inputs from CAM-chem-SD for each flight. Additionally, differences between GV OH and CAM-chem-SD OH may arise from differences in the OH precursor fields. This effect is examined by performing variable “swaps,” in which the box model is constrained by OH precursor fields from CAM-chem-SD except for a single input field taken instead from the GV observations. The resulting difference in OH between the “all CAM-chem-SD” box model run and the “all CAM-chem-SD + GV [variable]” run can then be ascribed to that precursor field. In this work, swap runs are performed using GV O<sub>3</sub>, H<sub>2</sub>O, NO<sub>x</sub> (NO + NO<sub>2</sub>), CO, C<sub>5</sub>H<sub>8</sub>, HCHO, CH<sub>3</sub>CHO, J(O<sup>1</sup>D), and J(NO<sub>2</sub>). These swap runs are performed for all flights.

The differences between GV OH and CAM-chem-SD OH are further quantified by calculating tropospheric column OH values. We integrate the 24 h mean OH number density ( $[OH]_{24 \text{ HR}}$ ) vertical profile, averaged for all flights, for each simulation of OH: GV OH, CAM-chem-SD OH (produced by the box model constrained to CAM-chem-SD precursors), and the swaps of the nine variables listed above. We also perform one additional simulation to examine the effect of a possible clear-sky sampling bias that occurred during aircraft sampling, discussed in section 3.1. In this simulation, we constrained the box model to J(NO<sub>2</sub>) and J(O<sup>1</sup>D) from CAM-chem-SD and GV observations for all other inputs. Columns are based on an integration from the surface to 13 km to match the vertical extent of columns calculated for the POLMIP CTM swap simulations (see section 3.3).

#### 2.4. POLMIP CTMs (2008)

POLMIP was conducted to utilize the Polar Study using Aircraft, Remote Sensing, Surface Measurements and Models, of Climate, Chemistry, Aerosols, and Transport (POLARCAT) [Law *et al.*, 2014] suite of observations acquired in 2008 for the purpose of evaluating global chemistry models [Emmons *et al.*, 2015]. While the POLARCAT aircraft campaigns focused on the Arctic troposphere, POLMIP consists of global model simulations. These simulations were performed for January to December 2008, using a common emissions inventory, with the exception of GEOS-Chem (see Emmons *et al.* [2015] for further detail). All participating models were run in CTM mode, meaning wind and temperature inputs are based on assimilated meteorological fields. Accordingly, meteorological variables are roughly consistent among the models. Each model was also run with its standard chemistry and deposition schemes. Models provided monthly mean output for many chemical, physical, and radiative variables, including OH. All models that provided a global field of OH—CAM4-chem [Lamarque *et al.*, 2012; Tilmes *et al.*, 2015], C-IFS [Flemming *et al.*, 2015], GEOS-Chem [Bey *et al.*, 2001; Mao *et al.*, 2010], GMI-GEOS5 [Duncan *et al.*, 2007; Strahan *et al.*, 2007], LMDZ-INCA [Hauglustaine *et al.*, 2004; Hourdin *et al.*, 2006], MOZART-4 [Emmons *et al.*, 2010], TM5 [Huijnen *et al.*, 2010; Williams *et al.*, 2013], and TOMCAT [Chipperfield, 2006]—are analyzed here. The POLMIP simulation of CAM4-chem does not include halogenated very short lived organic chemistry, as is included in CAM-chem-SD.

The POLMIP project and the CONTRAST campaign focused on different years, 2008 and 2014, respectively. The Multivariate El Niño–Southern Oscillation (ENSO) index for January/February 2008 was in a moderate negative phase while the same months in 2014 were neutral [Wolter and Timlin, 2011]. Hence, the westward shift of the Pacific warm pool in 2008 and associated changes in locations of active convection, biomass burning, and the northern subtropical jet stream could account for some of the differences between the POLMIP CTMs and CONTRAST observations. Variations in biomass burning, whether due to ENSO effects or other factors, could also account for differences in chemical species associated with fire emissions. However, fire count data obtained from the MODIS instrument on board the NASA Terra satellite indicate that biomass burning magnitude and distribution were similar in 2008 and 2014 (Figure S1 in the supporting

information). Furthermore, differences between the POLMIP multimodel mean of OH precursors and CONTRAST observations of these species are nearly identical to the differences between CAM-chem-SD (2014 meteorology) and CONTRAST. By extending our analysis to the POLMIP simulations, we are able to assess the strengths and a few shortcomings of a suite of CTMs. Finally, POLMIP output is available for all 12 months, allowing us to examine conditions in October, the month for which *Rex et al.* [2014] suggested that extremely low values of OH would be present in the TWP.

### 2.5. CH<sub>2</sub>Br<sub>2</sub> Lifetime

We use the 24 h average values of OH output from the box model constrained by GV observations and by the CAM-chem-SD model run performed for CONTRAST, as well as monthly mean OH from the POLMIP models, to evaluate the tropospheric lifetime of CH<sub>2</sub>Br<sub>2</sub>. This VSL bromocarbon is lost nearly exclusively by reaction with tropospheric OH. Here we use

$$k_{\text{OH}+\text{CH}_2\text{Br}_2} = 2.0 \times 10^{-12} \exp(-840/T) \text{cm}^3 \text{s}^{-1} \quad (1)$$

for the rate constant of reaction between OH and CH<sub>2</sub>Br<sub>2</sub> [*Sander et al.*, 2011], and the local lifetime (as a function of altitude) is found using

$$\tau_{\text{CH}_2\text{Br}_2}(z) = \frac{1}{k_{\text{OH}+\text{CH}_2\text{Br}_2}(z) \times [\text{OH}(z)]} \quad (2)$$

where [OH] is the number density of OH (units cm<sup>-3</sup>).

According to the *World Meteorological Organization* [2011] Scientific Assessment of Ozone Depletion, the global tropospheric mean lifetime of CH<sub>2</sub>Br<sub>2</sub> is 123 days. *Rex et al.* [2014] suggested that  $\tau_{\text{CH}_2\text{Br}_2}$  was ~188 days at 500 hPa in the TWP during October 2009, due to an OH minimum. We highlight the lifetime of CH<sub>2</sub>Br<sub>2</sub> below in order to further compare to the results of *Rex et al.* [2014].

### 2.6. HOLW Structures

We also evaluate the impact of high-O<sub>3</sub>, low-H<sub>2</sub>O (HOLW) structures on OH concentrations in the TWP. Many air parcels exhibiting high O<sub>3</sub> (defined as O<sub>3</sub> > 40 ppb) and low relative humidity (RH < 20%) were observed in the midtroposphere [*Pan et al.*, 2015; *Anderson et al.*, 2016]. Relative humidity is calculated from observed H<sub>2</sub>O and temperature (*T*), with respect to liquid water for *T* > 0°C and with respect to ice for *T* < 0°C. Primary production of OH occurs via (R1) followed by



The presence of HOLW structures, therefore, leads to competing effects on [OH]; low H<sub>2</sub>O tends to suppress [OH], while elevated O<sub>3</sub> drives production of O(<sup>1</sup>D) and OH. We use the box model to investigate the net effect on [OH] of HOLW structures and compare to the OH concentrations found in background conditions, defined here as O<sub>3</sub> < 25 ppb and RH > 70%.

## 3. Results and Discussion

### 3.1. GV and CAM-chem-SD OH, Research Flight 07

The GV run of the box model, in which all model inputs are taken directly from measurements made during CONTRAST, reveals OH mixing ratios that are generally higher than those calculated by the 2014 CAM-chem-SD simulation. Figures 2a and 2b show results from RF07, which occurred entirely within our latitude/longitude/SZA thresholds, conducted extensive vertical profiling, and provided mostly uninterrupted measurements of all chemical species and variables used to constrain the box model [see *Pan et al.*, 2016, Figure 5]. Figure 2a shows GV OH values calculated by the box model as circles overplotted on a “curtain” of OH values from CAM-chem-SD, in time and altitude. Figure 2b shows the correlation of GV OH against the OH value from CAM-chem-SD, extracted for the altitude of the observation. Based on the mean ratio of GV OH to CAM-chem-SD OH, CAM-chem-SD underestimates OH by about 60%. Considerable spread about the 1:1 line (*r*<sup>2</sup> = 0.12, Figure 2b) shows that the global model is not able to represent the variability of box modeled OH along the aircraft flight track.

To understand whether differences between the chemical mechanisms within DSMACC and CAM-chem-SD are contributing to the difference in OH shown in Figures 2a and 2b, we constrain the box model using inputs

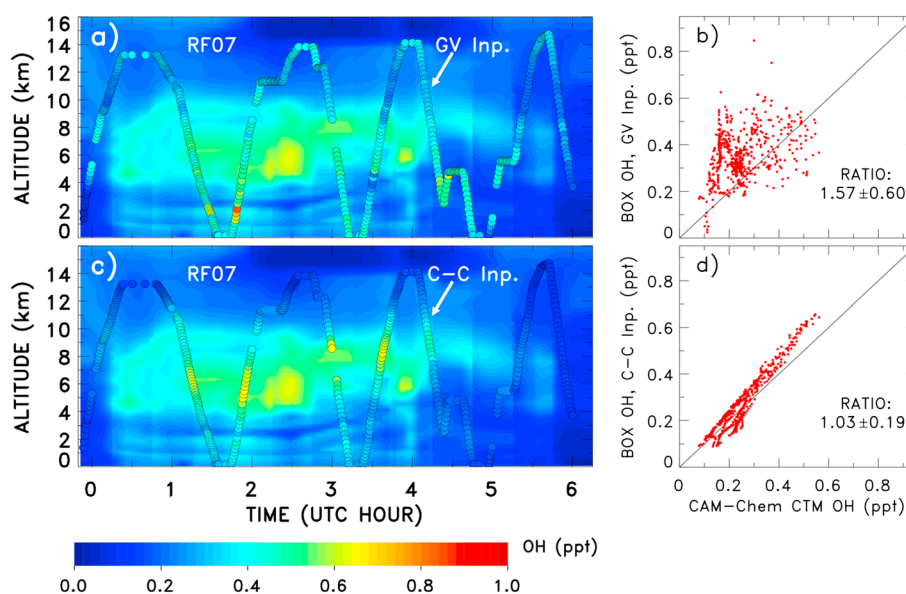


**Figure 2.** Box modeled OH compared to OH output from CAM-chem-SD run nudged to meteorology for the CONTRAST campaign; results here are for RF07 (29 January 2014): (a) the background curtain shows profiles of OH mixing ratios from CAM-chem-SD calculated for the latitude, longitude and SZA of the GV aircraft; the overplotted circles (GV Inp.) show OH output from the DSMACC box model constrained to CONTRAST observations; (b) scatterplot of box modeled OH versus CAM-chem-SD OH for the altitude of the GV; (c) same as Figure 2a but with box model (C-C Inp.) now constrained to OH precursors (section 2.2) from CAM-chem-SD; (d) same as Figure 2b but with box model constrained to OH precursors from CAM-chem-SD. The black line on the scatter plots is the 1:1 line. The mean and standard deviation of the ratio (BOX OH)/ (CAM-chem OH) are indicated.

of OH precursors from CAM-chem-SD. As shown in Figures 2c and 2d, the box model using CAM-chem-SD inputs does a much better job of matching CAM-chem-SD OH. The OH mixing ratios do not lie perfectly along the 1:1 line, suggesting that some differences in chemical mechanism may exist. However, the respective values of OH exhibit strong correlation ( $r^2 = 0.92$ ) and a mean ratio of  $1.03 \pm 0.19$ , demonstrating that the chemical mechanism does not drive the differences in OH seen in Figures 2a and 2b. A similar analysis for RF11, which sampled convective outflow to the south and southwest of Guam, is given in the supporting information (Figure S2). The results are very similar to those presented above for RF07.

Next we investigate each OH precursor using the box model “swap” method. Six variables,  $O_3$ ,  $H_2O$ ,  $J(O^1D)$ ,  $NO_x$ , HCHO, and  $CH_3CHO$ , account for the majority of the difference between GV and CAM-chem-SD OH for RF07. Figure 3 shows box model results for swaps of these six variables: i.e., the box model is constrained by the GV observation of the stated variable, while all other constraints are taken from CAM-chem-SD. Any deviation in the scatterplot from the tight linear correlation shown in the all CAM-chem-SD run (Figure 2d and grey points in Figure 3) results from differences in the swapped variable. The farther the new OH distribution (red points) is from the grey points, the larger the role of that variable in explaining the difference between GV and CAM-chem-SD OH. Also, the mean ratio of box model to CAM-chem-SD OH reported for each variable conveys the difference in OH resulting from the swap of the specified variable. In order of largest to smallest absolute difference, relative to CAM-chem-SD OH, we find that  $NO_x$ ,  $J(O^1D)$ ,  $H_2O$ , HCHO,  $O_3$ , and  $CH_3CHO$  drive the largest variations in OH. The variables CO,  $C_5H_8$ , and  $J(NO_2)$  do not have an appreciable effect on the difference between GV and CAM-chem-SD OH (Figure S3).

Figure 4 compares vertical profiles of  $NO_x$ ,  $J(O^1D)$ ,  $H_2O$ , HCHO,  $O_3$ , and  $CH_3CHO$  measured by the GV on RF07 to profiles along the GV flight track calculated using CAM-chem-SD. All panels represent mean and standard deviation of measured (GV, black) or modeled (CAM-chem-SD, red) profiles, except the  $NO_x$  panel. Here we have added observed NO and modeled  $NO_2$  found using the DSMACC model constrained to observed NO,  $O_3$ ,  $J(NO_2)$ , etc., to facilitate the evaluation of  $NO_x$  within CAM-chem-SD.

The abundance of  $NO_x$  is the most important driver of differences in GV and CAM-chem-SD OH. When the box model is constrained to observed NO, calculated OH is 61% higher than CAM-chem-SD OH (Figure 3d). The

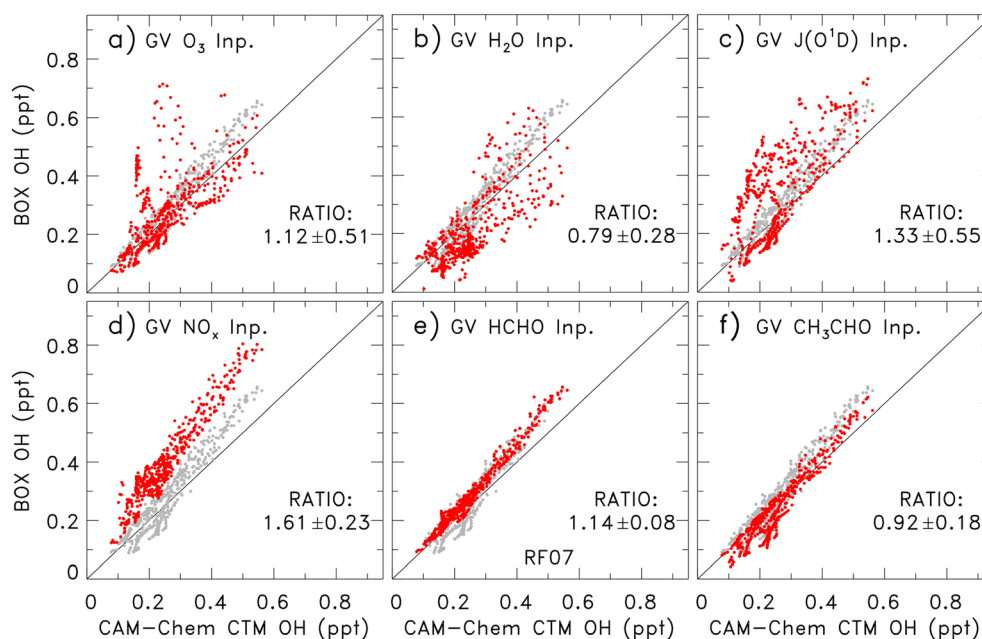


**Figure 3.** Same as scatterplots in Figure 2 except that the box model is constrained to output from CAM-chem-SD for all OH precursors with the exception of the precursor indicated by the label on each plot. Values for the labeled precursor are from CONTRAST (GV) observations obtained on RF07. The OH precursors constrained by measurements are (a)  $O_3$ , (b)  $H_2O$ , (c)  $J(O^1D)$ , (d)  $NO$  (with steady state  $NO_2$  calculated by the box model to give  $NO_x$ ), (e)  $HCHO$ , and (f)  $CH_3CHO$ . Grey points in the background are the same as the red points in Figure 2d, for the sake of visual comparison. The mean and standard deviation of the ratio (BOX OH)/(CAM-chem OH) are indicated.

profile of  $NO_x$  inferred from observed  $NO$  on RF07 is significantly larger than CAM-chem-SD  $NO_x$  throughout the troposphere (Figure 4d). As shown in section 3.2, the difference between measured and modeled  $NO_x$  is pervasive throughout the campaign. During CONTRAST, measurements of  $NO_y$  and reservoir species that link  $NO_x$  to  $NO_y$  were not obtained. As a result, it is not possible to ascertain whether the discrepancy between measured and modeled  $NO_x$  shown in Figure 4d would be reflected in a similar discrepancy for  $NO_y$ . Future observational campaigns in the TWP would benefit from observations of  $NO_y$  and a suite of nitrogen reservoir species.

The box model swaps indicate  $J(O^1D)$  has the second most important influence on OH for RF07. The mean ratio of OH calculated using GV  $J(O^1D)$  to OH from CAM-chem-SD is 1.33 (Figure 3c). The distribution of OH found using  $J(O^1D)$  from the GV and all other variables from CAM-chem-SD shows a clear elevation relative to CAM-chem-SD OH. Values of  $J(O^1D)$  observed during RF07 exceed values within CAM-chem-SD below  $\sim 8$  km (Figure 4c). This difference is due to the tendency of the GV to preferentially sample during clear-sky conditions: even though a primary goal of CONTRAST was the sampling of the outflow of active convection, the GV generally avoided flying either within or beneath active convection. This tendency for clear-sky sampling is evaluated further in section 3.2.

Differences in  $O_3$  and  $H_2O$ , related to the precise geographical location of HOLW structures in CAM-chem-SD, also drive the spread between GV and CAM-chem-SD OH (Figures 3a and 3b). The location and vertical extent of HOLW structures are determined by the interplay of biomass burning, long-range transport, and precipitation [Anderson *et al.*, 2016]. Mean profiles of  $O_3$  and  $H_2O$  from CAM-chem-SD agree well with mean profiles from the GV for RF07, especially in the midtroposphere around 3 to 5 km (Figures 4a and 4b). However, the model does not reproduce fine structure in  $O_3$  and  $H_2O$  along this flight track, which is not surprising given that CAM-chem-SD is a global model. This structure results in scatter when comparing OH from CAM-chem-SD to observations on a point-by-point basis (Figures 3a and 3b).

The remaining differences in OH for RF07, after accounting for the four variables above, are almost entirely explained by formaldehyde (HCHO) and acetaldehyde ( $CH_3CHO$ ). Constraining the box model to observations of HCHO results in a 14% increase above CAM-chem-SD OH (Figure 3e). While HCHO concentrations

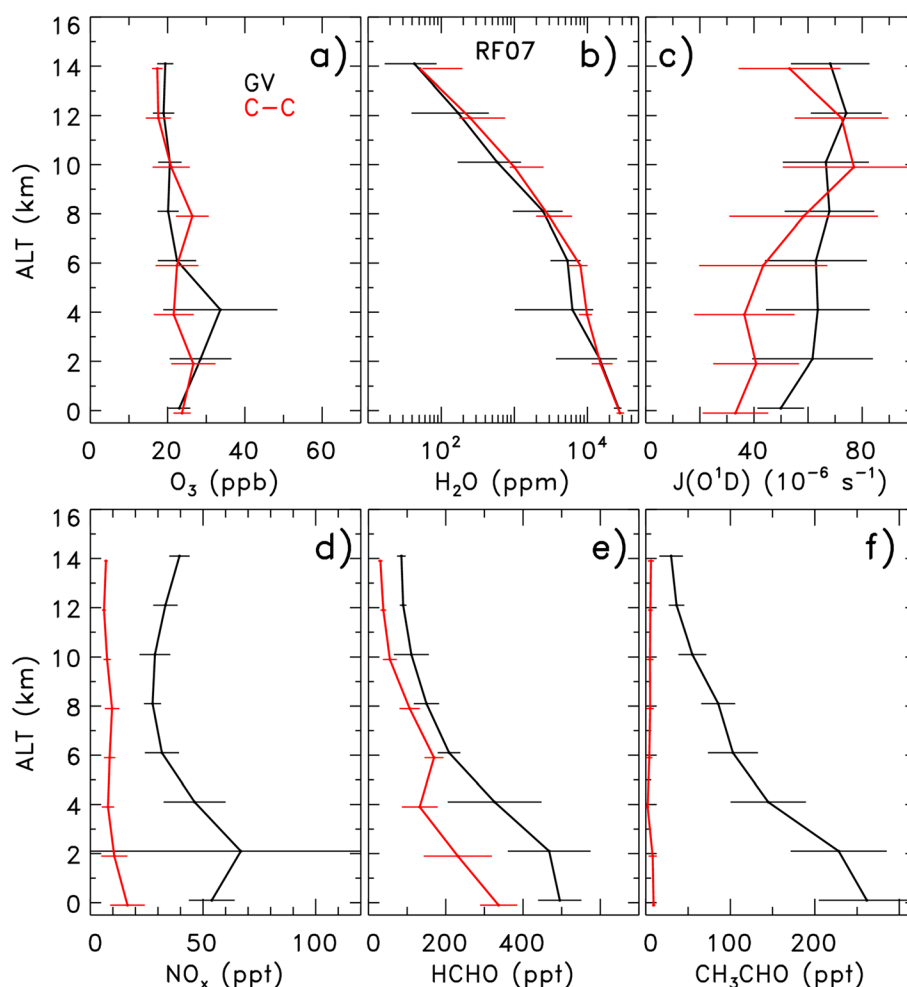


**Figure 4.** Vertical profiles of mean (a)  $\text{O}_3$ , (b)  $\text{H}_2\text{O}$ , (c)  $J(\text{O}^1\text{D})$ , (d)  $\text{NO}_x$ , (e)  $\text{HCHO}$ , and (f)  $\text{CH}_3\text{CHO}$  mixing ratios, averaged for CONTRAST RF07, subject to the selection filter for daytime TWP conditions described in section 2.1. GV observations are shown in black for all species except  $\text{NO}_x$ ; output from CAM-chem-SD, extracted along the flight track to match the time and location of GV observations, is shown in red. The GV  $\text{NO}_x$  is calculated using observed  $\text{NO}$  and box modeled  $\text{NO}_2$ , where the box model was constrained to GV observations of  $\text{NO}$ ,  $\text{O}_3$ ,  $J(\text{O}^1\text{D})$ , and hydrocarbons. Data and model output are averaged within 2 km altitude bins. Error bars show the standard deviation about the mean except for  $\text{H}_2\text{O}$ , where error bars show the 5th and 95th percentiles.

are underestimated by CAM-chem-SD throughout the troposphere (Figure 4e), most of the difference in OH resulting from the HCHO swap occurs in the upper troposphere, where OH mixing ratios are lowest. At the highest altitudes of GV sampling ( $\sim 14$  km), photolysis of HCHO constitutes one of the main sources of  $\text{HO}_x$  ( $\text{OH} + \text{HO}_2$ ) [Jaeglé *et al.*, 1998]. The larger concentrations of HCHO in the upper troposphere drive production of more OH than is calculated by CAM-chem-SD. Constraining the box model to GV  $\text{CH}_3\text{CHO}$ , on the other hand, results in an 8% decrease in OH (Figure 3f). CAM-chem-SD drastically underestimates observed concentrations of  $\text{CH}_3\text{CHO}$  (Figure 4f).

The underestimation of  $\text{CH}_3\text{CHO}$  in global models is a long-standing problem that could be due, in part, to the lack of oceanic emissions of this compound [Millet *et al.*, 2010; Read *et al.*, 2012]. None of the global models considered here represent oceanic emission of  $\text{CH}_3\text{CHO}$ . The inclusion of oceanic emission of this compound in global models has been shown to primarily affect abundances of  $\text{CH}_3\text{CHO}$  in the marine boundary layer, due to its short lifetime [Millet *et al.*, 2010; Read *et al.*, 2012]. The model underestimation of  $\text{CH}_3\text{CHO}$  throughout the troposphere shown in Figure 4f could also be due to underestimated primary emissions by biomass burning or misrepresentation of secondary production from the oxidation of VOC sources, such as ethane ( $\text{C}_2\text{H}_6$ ) and propane ( $\text{C}_3\text{H}_8$ ) [Millet *et al.*, 2010; Read *et al.*, 2012].

In addition to the six OH precursors discussed above, observed values of CO, C<sub>5</sub>H<sub>8</sub>, and J(NO<sub>2</sub>), were also analyzed using the box model swap method. These variables exhibit little influence on modeled OH. Swaps for each of these variables for RF07 show structures and correlations similar to the box model simulation constrained only to inputs from CAM-chem-SD (Figure S3). When each observed OH precursor is considered as a constraint in isolation, the sum of the effects on box modeled OH (as examined through the mean ratio statistic) does not exactly match the effect on OH found by constraining the box model to observations of all OH precursors simultaneously. The chemical impacts of these variables on OH are coupled to some extent. The linear combination of individual effects suggests an even larger increase in the ratio of GV OH to CAM-chem-SD OH than is found by the simulation that considers simultaneous variable swaps.

To put these results in context, we have evaluated the effect of measurement uncertainties of OH precursors on the box model calculation of GV OH. Details are shown in Figure S4. The 1 $\sigma$  uncertainty in GV OH found using a root sum of squares propagation of measurement uncertainties in the OH precursors is  $\pm 14\%$ . Uncertainty in the measurement of NO is the largest single contributor,  $\pm 10\%$ , to the total uncertainty. This uncertainty is much smaller than the difference in GV and CAM-chem-SD OH (Figure 2b), as well as the variability in OH mixing ratio driven by geophysically plausible variations in the precursor fields. Consequently, the error bars used below are based on standard deviation about the mean (i.e., when binning the data with respect to altitude).

### 3.2. GV and CAM-chem-SD OH, Campaign-Wide Results

Consideration of GV and CAM-chem-SD OH for all CONTRAST flights produces results similar to those shown above for RF07. Figure 5 shows scatterplots of GV OH versus CAM-chem-SD OH (Figure 5a) as well as OH calculated by the box model constrained to all precursors from CAM-chem-SD versus CAM-chem-SD OH (Figure 5b). Figures 5c and 5d show corresponding plots, for [OH] in units of number density. Results in this figure and those to follow are subject to the latitude, longitude, and SZA filter described in section 2.1 (i.e., sunlit measurements in the TWP). Figure 6 compares vertical profiles of NO<sub>x</sub>, J(O<sup>1</sup>D), H<sub>2</sub>O, HCHO, O<sub>3</sub>, and CH<sub>3</sub>CHO measured by the GV for the entire CONTRAST campaign, RFs 04–15, to profiles found using CAM-chem-SD, sampled along the GV flight track. Finally, Table 1 summarizes the effect of variable swaps on tropospheric column OH (OH<sup>COL</sup>) for the entire campaign. We have chosen to tabulate OH<sup>COL</sup> because this is the most important quantity for the oxidative capacity of the tropical troposphere. Tropospheric column OH is integrated from the surface to 13 km, because this is the altitude range extensively sampled by the GV aircraft. The profile of [OH]<sub>24 HR</sub> falls off between 13 km and the tropopause, so this definition captures most of the oxidative capacity of the tropical troposphere.

The mean ratio of GV OH to CAM-chem-SD OH mixing ratio for the entire campaign is  $1.40 \pm 0.58$ , indicating that OH constrained by the CONTRAST observations is on average 40% higher than CAM-chem-SD OH (Figure 5a). We test the effect of filling in missing data (section 2.2) by restricting this analysis to GV OH calculated only for the 311 data points where observations of all box model inputs are available (not shown). The resulting mean ratio of GV OH to CAM-chem-SD OH is  $1.52 \pm 0.59$ , suggesting that our findings are not influenced by our treatment of the data. Constraining the box model to OH precursors from CAM-chem-SD results in a mean ratio of  $1.03 \pm 0.19$  (Figure 5b). The comparison shown in Figure 5b demonstrates similarity of the chemical mechanism for representation of tropospheric OH between DSMACC and CAM-chem-SD. The most notable differences are at high OH mixing ratios, which occur in the midtroposphere.

It is important to also examine OH number density ([OH]). Even though many studies of tropospheric OH rely on mixing ratio [e.g., Brune *et al.*, 1998; Jaeglé *et al.*, 1998; Olson *et al.*, 2004], the lifetime of species lost by reaction with OH is determined by [OH]. Figure 5c shows the ratio of GV and CAM-chem-SD [OH] is slightly less than found for the OH mixing ratio, because number density places a higher weight on observations in the middle and lower troposphere. Constraining the box model to precursors from CAM-chem-SD also results in a mean ratio of  $1.03 \pm 0.19$  for [OH] (Figure 5d). However, this ratio is weighted heavily toward the lowest values of [OH] (between  $1 \times 10^6$  and  $5 \times 10^6$  cm<sup>-2</sup>) due to more frequent aircraft sampling at high altitudes. Recalculating this ratio using a binning approach (grey points, Figure 5d) places equal weight on all values of [OH]. The ratio of the grey points is  $1.13 \pm 0.15$ , which is consistent with the visual interpretation of Figure 5d. The slope of a linear fit forced to go through the origin is 1.15 (we use this approach since negative OH is non-physical). We conclude that the effect of differences between the DSMACC and CAM-chem-SD chemical mechanisms on [OH] lies between 3% and 15%. In the POLMIP section, we make an adjustment to the box

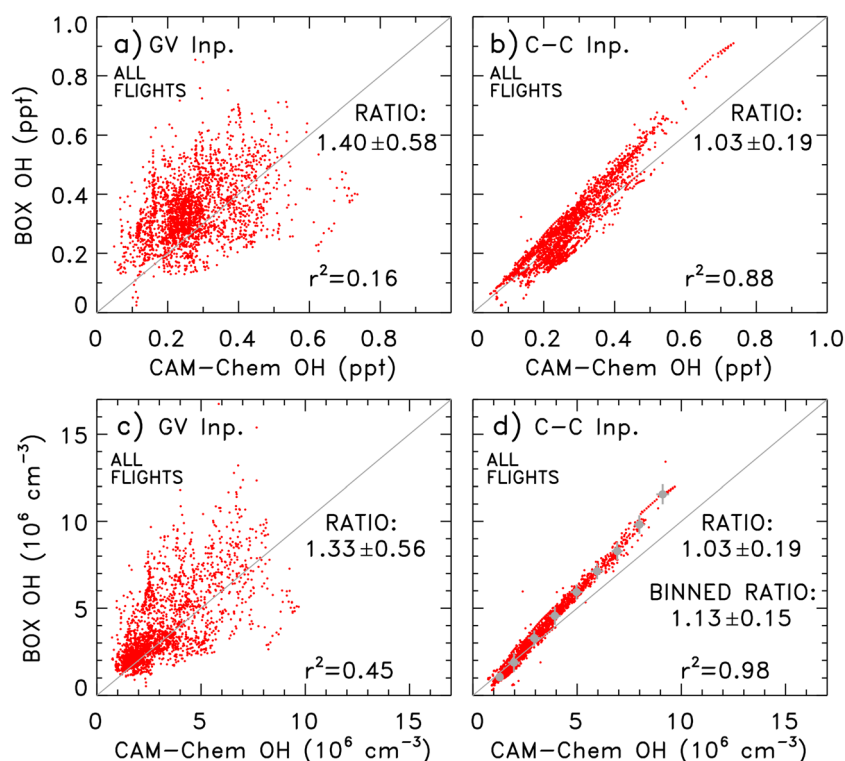


**Figure 5.** Correlation plots of box modeled OH versus CAM-chem-SD OH for the entire CONTRAST campaign, with application of the filter used to select daytime observations in the TWP (section 2.1). (a) Box modeled OH found using constraints for OH precursors from the CONTRAST GV observations; (b) box modeled OH found using constraints from CAM-chem-SD. (c and d) Same as Figures 5a and 5b, respectively, except that OH is represented as number density instead of mixing ratio. The square of the correlation coefficient ( $r^2$ ) and the mean and standard deviation of the ratio (BOX OH)/(CAM-chem OH) are indicated. Figure 5d also shows statistics performed by averaging the CAM-chem OH values within  $1 \times 10^6 \text{ cm}^{-3}$  interval bins; the mean BOX OH values are determined for those bins, and the resulting mean and standard deviations are shown in grey. The ratio of (BOX OH)/(CAM-chem OH) for the grey points is indicated as the “binned ratio.”

model based on the 1.13 ratio, because this is the most reliable measure of the difference in the chemical mechanism between DSMACC and CAM-chem-SD.

The first two rows of Table 1 show that  $\text{OH}^{\text{COL}}$  based on the mean vertical profile campaign-wide GV OH is 12% higher than  $\text{OH}^{\text{COL}}$  found using CAM-chem-SD inputs within the box model. The other rows of Table 1 show the impact on  $\text{OH}^{\text{COL}}$  of the various precursors. The first numerical entry shows  $\text{OH}^{\text{COL}}$  resulting from using the GV measurement of the specific OH precursor within the box model, with all other precursors based on CAM-chem-SD. The other numerical entry shows the ratio of  $\text{OH}^{\text{COL}}$  resulting from the variable swap divided by  $1.94 \times 10^{12} \text{ cm}^{-2}$ , the value of  $\text{OH}^{\text{COL}}$  from CAM-chem-SD.

As noted above, the GV tended to sample in clear-sky conditions during CONTRAST. This tendency accounts for nearly all of the difference between  $\text{OH}^{\text{COL}}$  found using GV OH precursors and those from CAM-chem-SD. Use of  $J(\text{O}^1\text{D})$  and  $J(\text{NO}_2)$  from CAM-chem-SD, and all other precursors from GV, results in  $\text{OH}^{\text{COL}} = 1.92 \times 10^{12} \text{ cm}^{-2}$  (last entry, Table 1), which is nearly identical to  $\text{OH}^{\text{COL}}$  based on use of precursors exclusively from CAM-chem-SD. Hence,  $\text{OH}^{\text{COL}}$  inferred from campaign-wide sampling of the TWP is in remarkably good agreement with that of CAM-chem-SD. Nonetheless, there are important differences for the various precursors that tend to cancel out. Next, we examine the effect of individual precursors on  $\text{OH}^{\text{COL}}$ .

Vertical profiles of  $\text{O}_3$ ,  $\text{H}_2\text{O}$ ,  $J(\text{O}^1\text{D})$ ,  $\text{NO}_x$ ,  $\text{HCHO}$ , and  $\text{CH}_3\text{CHO}$  for the entire campaign compared to CAM-chem-SD (Figure 6) exhibit similar differences as shown for RF07 (Figure 4). Measured and modeled profiles of  $\text{O}_3$  agree very well throughout the campaign (Figure 6a) even though a considerable portion of the scatter in Figure 5 is due to  $\text{O}_3$ . CAM-chem-SD accurately represents the impact on  $\text{O}_3$  of biomass burning and transport processes on the synoptic scale. However, the model cannot be expected to reproduce atmospheric  $\text{O}_3$  on the

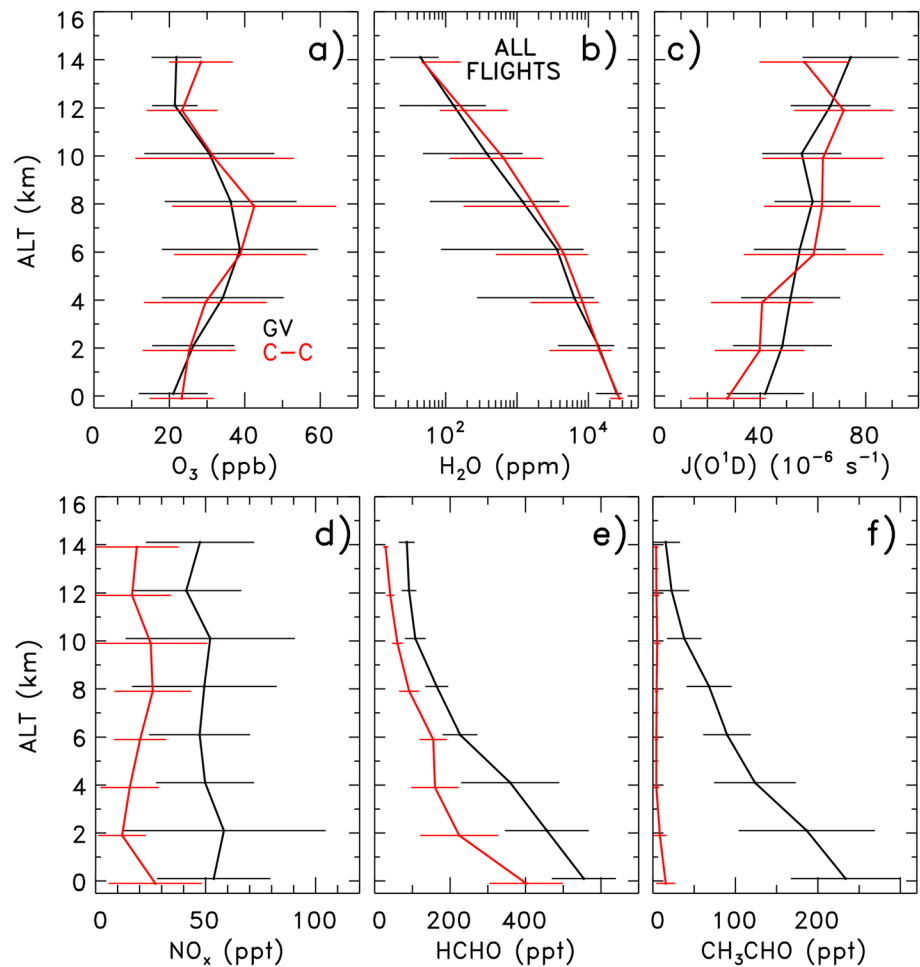


**Figure 6.** Same as Figure 4 except that vertical profiles are calculated for the entire CONTRAST campaign, subject to the time and location filter described in section 2.1.

convective scale, so structures in  $O_3$  are offset in space and time relative to aircraft observations. Use of GV  $O_3$  results in a 6% increase of  $OH^{COL}$  compared to the baseline simulation (all precursors from CAM-chem-SD).

The measured profile of  $H_2O$  throughout the campaign tends to be ~20% lower than the profile of  $H_2O$  within CAM-chem-SD (Figure 6b), resulting in a 17% decrease in  $OH^{COL}$  (Table 1) compared to the baseline.

Relative humidity in the TWP exhibits a bimodal distribution, with high RH (>70%) characterizing air masses recently influenced by local convection and low RH (<20%) for aged air parcels [Anderson et al., 2016]. The differences in  $H_2O$  shown in Figure 6b could reflect either the treatment of RH upon detrainment from deep convection within CAM-chem-SD or the representation of aged air parcels. Regardless, substitution of GV  $O_3$  and  $H_2O$  for CAM-chem-SD  $O_3$  and  $H_2O$  within the DSMACC box model results in only an 11% decline in  $OH^{COL}$ .

**Table 1.** Tropospheric OH Columns Calculated for the CONTRAST Mean OH Vertical Profile and CAM-Chem-SD Model Simulations

C-C Box Model Run	OH Column ( $10^{12} \text{ cm}^{-2}$ ) <sup>a</sup>	Ratio (Run X/C-C)
GV	2.17	1.12
C-C (CONTRAST)	1.94	---
C-C, GV $NO_x$	2.61	1.35
C-C, GV $H_2O$	1.61	0.83
C-C, GV $J(O^1D)$	2.16	1.11
C-C, GV $CH_3CHO$	1.77	0.91
C-C, GV $O_3$	2.06	1.06
C-C, GV CO	1.83	0.94
C-C, GV HCHO	2.01	1.04
C-C, GV $J(NO_2)$	1.97	1.02
C-C, GV $C_5H_8$	1.95	1.01
GV, C-C $J(O^1D) + J(NO_2)$	1.92	0.99

<sup>a</sup>Columns are integrated from the surface to 13 km (~200 hPa).

The measured profile of  $\text{NO}_x$  is more than a factor of 2 larger than found within CAM-chem-SD (Figure 6d). Use of observed NO within the box model results in a 35% rise in  $\text{OH}^{\text{COL}}$  relative to baseline. As shown in section 3.3, the POLMIP CTMs also underestimate observed  $\text{NO}_x$  by a similar amount. A possible explanation is that emissions of  $\text{NO}_x$  from biomass burning regions are underestimated by the FINN emission inventory used to drive CAM-chem-SD. If so, the various emission inventories used to drive the POLMIP CTMs likely suffer from the same deficit. Additionally, lightning over Africa is responsible for a large source of  $\text{NO}_x$  in the upper troposphere that is likely transported to the TWP following the same pathway as biomass burning plumes [Jacob *et al.*, 1996; Murray *et al.*, 2013; Anderson *et al.*, 2016]. Also,  $\text{NO}_x$  is converted to peroxyacetyl nitrate (PAN) during transit from Africa and Southeast Asia to the TWP [Singh and Hanst, 1981]. Biomass burning plumes descend as they transit from Africa and Southeast Asia to the TWP [Anderson *et al.*, 2016]. As an air parcel descends,  $\text{NO}_x$  is regenerated upon thermal decomposition of PAN. The GV payload during CONTRAST only measured NO within the  $\text{NO}_y$  family, so it is not possible to assess whether the  $\text{NO}_x$  deficit within CAM-chem-SD (and the POLMIP CTMs) is due to speciation of reactive nitrogen compounds. The  $\text{NO}_x$  deficit is important to resolve because low  $\text{NO}_x$  is the largest driver of differences between GV OH and OH found by global models.

As noted for RF07, the campaign-wide mean vertical profile of acetaldehyde ( $\text{CH}_3\text{CHO}$ ) within CAM-chem-SD is much lower than observed (Figure 6f). Analysis of the atmospheric budget of  $\text{CH}_3\text{CHO}$  indicates that the deficit may result from missing oceanic sources [Singh *et al.*, 2003, 2004; Millet *et al.*, 2010; Read *et al.*, 2012] and poor representation of primary and secondary production of  $\text{CH}_3\text{CHO}$  [Millet *et al.*, 2010; Read *et al.*, 2012] as noted previously. The use of observed  $\text{CH}_3\text{CHO}$  within the box model results in a 9% decline in  $\text{OH}^{\text{COL}}$  relative to baseline, because this compound is a sink for OH. The effect on OH is largest in the lower troposphere. However,  $\text{CH}_3\text{CHO}$  is a source of HCHO [Singh *et al.*, 2004] and this may explain some of the underprediction of HCHO by CAM-chem-SD. Constraining the calculation of  $\text{OH}^{\text{COL}}$  to observed HCHO results in a 4% rise. The production and loss processes of HCHO observed during CONTRAST will be published separately (D. C. Anderson *et al.*, manuscript in preparation).

The entries in Table 1 for CO and isoprene ( $\text{C}_5\text{H}_8$ ) confirm, as found for RF07, that these two compounds have a small effect on differences between CAM-chem-SD and GV  $\text{OH}^{\text{COL}}$  in the TWP. The use of observed CO within the box model results in a 6% decline in  $\text{OH}^{\text{COL}}$  relative to baseline, while the use of observed  $\text{C}_5\text{H}_8$  causes a 1% increase in  $\text{OH}^{\text{COL}}$ . Although CAM-chem-SD significantly underestimates the observed mean vertical profile of CO (Figure S5a), the response of OH to this difference is small. The response of OH to differences in  $\text{C}_5\text{H}_8$  is negligible due to the near-zero concentrations of the compound, evident in GV observations and CAM-chem-SD output (Figure S5b).

We now transition to analyzing 24 h average OH values calculated as vertical profiles of the campaign-wide results. Vertical distributions of 24 h average OH provide the context for interpreting our results in a manner that is meaningful for examining the oxidizing capacity of the troposphere. Our calculations of vertical, 24 h mean GV OH and CAM-chem-SD indicate that the largest differences occur in the lower (below  $\sim 4$  km) and upper (above  $\sim 10$  km) troposphere (Figures 7a and 7b). Figure 7a shows 24 h average mixing ratios of OH ( $[\text{OH}_{24 \text{ HR}}]$ ), and Figure 7b shows 24 h average  $[\text{OH}]$  ( $[\text{OH}_{24 \text{ HR}}]$ ). We show both mixing ratio and number density for the convenience of the atmospheric chemistry community, since both measures are commonly used. Here CAM-chem-SD  $[\text{OH}_{24 \text{ HR}}]$  and  $[\text{OH}_{24 \text{ HR}}]$  is based on the diel steady state output of the DSMACC box model, constrained to OH precursors from CAM-chem-SD, because 24 h average OH was not available from CAM-chem-SD. We make no attempt to adjust for the possible difference in chemical mechanism between DSMACC and CAM-chem-SD. Since DSMACC overestimates daytime  $[\text{OH}]$  by 3 to 13% compared to CAM-chem-SD (Figure 5d), it is possible that CAM-chem-SD  $[\text{OH}_{24 \text{ HR}}]$  is 1.5 to 6.5% higher than actual 24 h average OH from CAM-chem-SD (because values of daytime  $[\text{OH}]$  are roughly twice values of  $[\text{OH}_{24 \text{ HR}}]$ ). This difference is smaller than the standard deviation about the mean of the various profiles.

Figure 7b shows that most of the 12% difference in  $\text{OH}^{\text{COL}}$  between GV and CAM-chem-SD is due to the tendency for  $[\text{OH}_{24 \text{ HR}}]$  from GV to exceed that from CAM-chem-SD below  $\sim 5$  km. This  $[\text{OH}_{24 \text{ HR}}]$  difference at low altitudes is primarily a result of the observation of much higher levels of  $\text{NO}_x$  than found by CAM-chem-SD (Figure 6d). The tendency for  $J(\text{O}^1\text{D})$  from the GV to exceed that within CAM-chem-SD (Figure 6c) also contributes to the low-altitude difference. The good agreement between GV and CAM-chem-SD  $[\text{OH}_{24 \text{ HR}}]$  in the midtroposphere occurs despite the CAM-chem-SD underestimation of  $\text{NO}_x$ ; the effects of underestimated

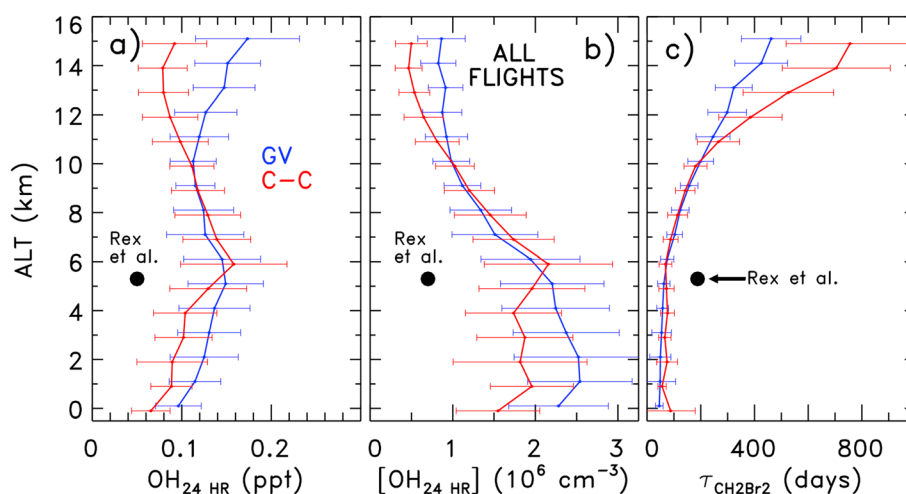


**Figure 7.** The 24 h average OH ( $\text{OH}_{24 \text{ HR}}$ ) and lifetime of  $\text{CH}_2\text{Br}_2$  ( $\tau_{\text{CH}_2\text{Br}_2}$ ) from the DSMACC box model for the entire CONTRAST campaign, subject to the time and location filter described in section 2.1, separated into 1 km altitude bins. (a)  $\text{OH}_{24 \text{ HR}}$  mixing ratio, (b)  $\text{OH}_{24 \text{ HR}}$  number density, and (c)  $\tau_{\text{CH}_2\text{Br}_2}$  with respect to loss by OH. Blue line denotes box model  $\text{OH}_{24 \text{ HR}}$  and  $\tau_{\text{CH}_2\text{Br}_2}$  for runs constrained to GV measurements; red line denotes box model  $\text{OH}_{24 \text{ HR}}$  for runs constrained to CAM-chem-SD output. Error bars signify standard deviation about the mean of  $\text{OH}_{24 \text{ HR}}$  and  $\tau_{\text{CH}_2\text{Br}_2}$ , for each altitude bin. Error bars are offset slightly in altitude for clarity. We also show  $\text{OH}_{24 \text{ HR}}$  and  $\tau_{\text{CH}_2\text{Br}_2}$  at 500 hPa (which we place at 5.3 km altitude) reported by Rex *et al.* [2014] above the equator on 1 October 2009.

$\text{H}_2\text{O}$  compensate by decreasing OH in the 5 to 10 km range. Interestingly, as detailed in the supporting information (Figure S6), we calculate less  $\text{OH}_{24 \text{ HR}}$  within high  $\text{O}_3$ /low  $\text{H}_2\text{O}$  (HOLW) structures relative to background between 3 and 10 km, because low  $\text{H}_2\text{O}$  (suppresses primary production of  $\text{HO}_x$ ) has a larger effect on  $\text{OH}_{24 \text{ HR}}$  than the combination of high  $\text{O}_3$  (increases primary production of  $\text{HO}_x$ ) and elevated  $\text{NO}_x$  (increases secondary production OH). While this is true in the midtroposphere, the effect of HOLW structures on OH above  $\sim 10$  km switches to increase radical concentrations over background. This occurs with a sharp increase in concentrations of  $\text{NO}_x$  (Figure S6b).

Crawford *et al.* [1997] also noted a sharp increase in  $\text{NO}_x$  at  $\sim 10$  km in the TWP during the PEM-West B campaign (February and March 1994), where maximum concentrations of  $\text{NO}_x$  of  $\sim 70$  ppt were observed at the highest sampled altitude bin of 8–10 km. Concentrations of  $\text{NO}_x$  from CONTRAST reach values nearly double the value from Crawford *et al.* [1997]. We attribute enhanced  $\text{NO}_x$  in the HOLW structures to tropical biomass burning [Anderson *et al.*, 2016], whereas Crawford *et al.* [1997] concluded that lightning was the primary source of enhanced  $\text{NO}_x$ . Increases in biomass burning between 1994 and 2014 may explain the differences in  $\text{NO}_x$  between these two studies.

Figure 7a shows considerable differences in  $\text{OH}_{24 \text{ HR}}$  mixing ratio in the upper troposphere. As expected, the upper troposphere exhibits smaller absolute differences for  $[\text{OH}_{24 \text{ HR}}]$  (Figure 7b) and makes only a small contribution to  $\text{OH}^{\text{COL}}$ . This upper tropospheric difference is a result of the observation of considerably higher levels of HCHO (Figure 6e) and  $\text{NO}_x$  (Figure 6d) compared to CAM-chem-SD. The upper troposphere is extremely important, even though there is a small effect on  $\text{OH}^{\text{COL}}$ , because energetic convection in the TWP often detrains at this level [e.g., Pan *et al.*, 2016, Figure 9].

Figure 7c shows vertical profiles of  $\tau_{\text{CH}_2\text{Br}_2}$  found using equation (2) as well as the value for  $\tau_{\text{CH}_2\text{Br}_2}$  at 500 hPa ( $\sim 5.3$  km) of 188 days given by Rex *et al.* [2014]. We also show values of  $\text{OH}_{24 \text{ HR}}$  mixing ratio (Figure 7a) and  $[\text{OH}_{24 \text{ HR}}]$  (Figure 7b) at this vertical level from Rex *et al.* [2014]. The values from Rex *et al.* [2014] are based on model calculations and ozonesonde observations in the TWP conducted during October 2009. In section 3.3, we show comparisons to POLMIP results for October 2008.

Rex *et al.* [2014] suggested that the occurrence of very low OH in the TWP (black circle in Figures 7a and 7b) was driven by mixing ratios of  $\text{O}_3$  lying close to zero and well below 20 ppbv, based on ozonesonde observations and supported by output from GEOS-Chem [Ridder *et al.*, 2012]. Newton *et al.* [2016] focused on details of ozonesonde calibration as a possible explanation for the near-zero levels of  $\text{O}_3$  reported by Rex *et al.* [2014].

However, it is unclear why GEOS-Chem v8-02-04, used by Ridder *et al.*, demonstrates good agreement with the ozonesonde measurements. Calculations of tropospheric O<sub>3</sub> columns from the v9-01-03 simulation of GEOS-Chem conducted for POLMIP, as well as tropospheric column O<sub>3</sub> from the other POLMIP CTMs, do not support the values of <15 DU of this quantity from GEOS-Chem near Guam shown by Rex *et al.* [2014] (Figure S7a). The one exception is the TOMCAT model, which reaches tropospheric O<sub>3</sub> column values of ~13.5 DU in the months of August and September near Guam. One change implemented in the version of GEOS-Chem used in our study is improved treatment of the yield of isoprene nitrates in the isoprene oxidation mechanism [Mao *et al.*, 2013a]. The downward revision of the isoprene nitrate yield results in an increase in the ozone production efficiency, which could be responsible for a small part of the difference for O<sub>3</sub> in the TWP found here, compared to the GEOS-Chem results of Ridder *et al.* and Rex *et al.* The GEOS-Chem group maintains a benchmark of model output for year 2005 found using various versions of this model. As shown in Figure S7b, tropospheric column O<sub>3</sub> in the TWP during October 2005 is quite similar for v8-02-04 and v9-01-03 of GEOS-Chem. All of these values are much higher than tropospheric column O<sub>3</sub> in the TWP during October 2008 reported by Ridder *et al.* and Rex *et al.*

Another explanation for low OH in the TWP offered by Gao *et al.* [2014] and Rex *et al.* [2014] is very small abundance of NO<sub>x</sub>. Low NO<sub>x</sub> can suppress OH, as HO<sub>2</sub> tends to preferentially exist as HO<sub>2</sub> rather than OH under this condition. However, concentrations of NO observed during CONTRAST rarely reached the extremely low values reported by Gao *et al.* [2014] and noted by Rex *et al.* [2014] (CONTRAST [NO] was less than  $1 \times 10^8 \text{ cm}^{-3}$  only 3.5% of the time for the altitude range 9 to 15 km; Figure S8).

The GV observations of OH precursors suggest that the lifetime of CH<sub>2</sub>Br<sub>2</sub> at 500 hPa (~5.3 km) is ~66 days, nearly a factor of 3 lower than the Rex *et al.* [2014] estimate of ~188 days. Consequently, loss of CH<sub>2</sub>Br<sub>2</sub> could occur in the middle troposphere for air masses that detrain at this level. Observations of the vertical profile of CH<sub>2</sub>Br<sub>2</sub> observed by the TOGA instrument show a slight local minimum in the middle troposphere, possibly suggesting local photochemical loss (Figure S9). However, the lifetime of CH<sub>2</sub>Br<sub>2</sub> based on CONTRAST observations rises to ~200 days at 10 km and exceeds 400 days above 14 km, due to the falloff of [OH]<sub>24 HR</sub> (Figure 7). Since convection driven by the TWP warm pool often detrains above 10 km, significant injection of CH<sub>2</sub>Br<sub>2</sub> to the lowermost stratosphere is expected, as was observed during the NASA Airborne Tropical Tropopause Experiment campaign [Navarro *et al.*, 2015].

### 3.3. Comparison to POLMIP Models

We extend our analysis of OH in the TWP to the POLMIP simulations, since the output from these CTMs is available for all 12 months. These comparisons allow us to examine conditions in October, the month for which Rex *et al.* [2014] suggested that extremely low values of OH would be present in the TWP. The POLMIP runs used meteorology and emissions for 2008, and the archive consists of monthly mean fields [Emmons *et al.*, 2015]. As detailed below, conclusions drawn from the POLMIP comparisons are consistent with the findings based on the comparison to CAM-chem-SD run for winter 2014 (sections 3.1 and 3.2).

Figures 8 and 9 show comparisons of POLMIP monthly mean OH mixing ratio, OH number density ([OH]), as well as OH precursors and related species to 24 h average values of these quantities inferred from GV measurements during CONTRAST. Figures 8a–8e and 9a–9e show results from individual CTMs, whereas the Figures 8f–8j and 9f–9j show results from the POLMIP multimodel mean (POL MMM). All POLMIP results shown in these two figures use the average of January and February 2008 monthly means for all model output that lies within the TWP boundary region shown in Figure 1; i.e., the 2008 POLMIP archive is sampled at the same season and location as the CONTRAST campaign. The vertical coordinate of pressure is used because the POLMIP archive only provided output on a pressure grid. For the diurnally varying quantities OH, NO<sub>x</sub>, J(O<sup>1</sup>D), and J(NO<sub>2</sub>), the 24 h average values from CONTRAST are campaign-wide averages of the 24 h average output of DSMACC box model runs constrained to aircraft observations, whereas for HCHO the estimate of 24 h average value is based on scaling factors from the University of Washington Chemical Model (UWCM) model [Wolfe and Thornton, 2011] in which HCHO concentrations vary diurnally (which is not the case for the DSMACC box model). Additionally, POLMIP values of isoprene (C<sub>5</sub>H<sub>8</sub>) are represented in Figure 8e as the median C<sub>5</sub>H<sub>8</sub> concentrations from the individual models and in Figure 8j as the multimodel mean of those median values. This is done to prevent the non-Gaussian distribution of C<sub>5</sub>H<sub>8</sub> concentrations, influenced by transport of air with high C<sub>5</sub>H<sub>8</sub> from nearby landmasses, from exerting an artificial high bias.

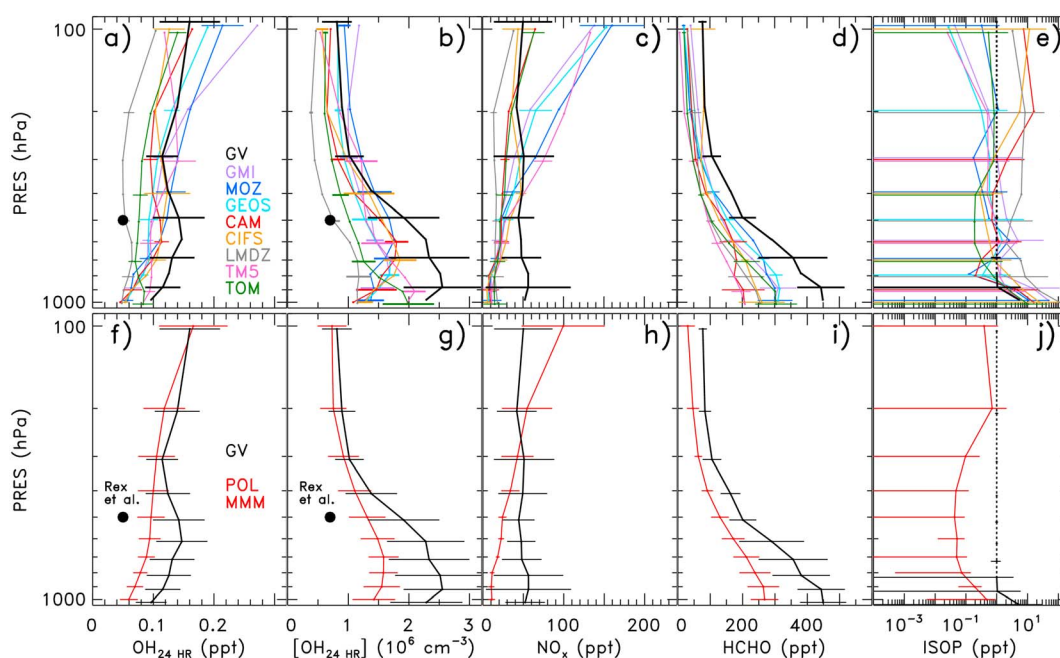


**Figure 8.** Vertical profiles of monthly mean (a, f) OH mixing ratio, (b, g) OH concentration, (c, h)  $\text{NO}_x$ , (d, i) HCHO, and (e, j)  $\text{C}_5\text{H}_8$  from the POLMIP archive for eight CTMs (colored lines) for January and February 2008 averaged within the TWP region shown in Figure 1. The black solid lines, described in greater detail below, represent either inferred OH or GV observations. The upper set of panels shows profiles from each POLMIP CTM, while the lower set shows the POLMIP multimodel mean. Error bars show 1 standard deviation about the mean of the various quantities, in 100 hPa pressure bins; they are offset slightly in the vertical for clarity. For the top panels, some of the error bars are omitted to avoid clutter. The black solid lines show 24 h mean OH mixing ratio (Figures 8a and 8f) and OH concentration (Figures 8b and 8g) output from the DSMACC box model constrained by GV inputs. The same latitude/longitude filter, specific to the TWP, has been applied to the POLMIP archive and inferred OH values. The OH panels also show the October 2009 value at 500 hPa in the TWP from *Rex et al.* [2014]. The black solid lines for  $\text{NO}_x$  are 24 h averages of the diel output of NO plus  $\text{NO}_2$  from DSMACC, for calculations constrained to match observed NO at the SZA of observation. The black solid lines for HCHO also represent 24 h average values, which in this case are found by scaling the observed HCHO to  $\text{HCHO}_{24\text{ HR}}$  using the UWCM chemical box model (see text). The scaling for HCHO is close to unity at all altitudes because the photochemical lifetime of HCHO is on the order of a few hours (see supporting information). The CTM/observation comparison for  $\text{C}_5\text{H}_8$  (ISOP) is handled in a different manner. Figure 8e compares the mean and standard deviation from each CTM to the observed mean and standard deviation; often,  $\text{C}_5\text{H}_8$  was below the limit of detection of the TOGA instrument, 1 ppt, because our analysis is focused on the remote TWP. The black dotted line depicts the instrument limit of detection for pressure bins where this is the case.  $\text{C}_5\text{H}_8$  from the POLMIP CTMs in Figure 8j (red line) is represented as the multimodel mean of the median values, due to the non-Gaussian distribution of values in the TWP region.

The profiles of monthly mean OH in the TWP for boreal winter 2008 from the individual POLMIP models (Figures 8a and 8b) all lie below the campaign-wide GV-based  $\text{OH}_{24\text{ HR}}$  profile, from the surface to  $\sim 500$  hPa (about 5 km). There is considerable variation in monthly mean OH in the TWP among the POLMIP models, which is consistent with the results of other model intercomparison studies [*Shindell et al.*, 2006; *Fiore et al.*, 2009; *Voulgarakis et al.*, 2013]. We also show the *Rex et al.* [2014] estimate of  $\text{OH}_{24\text{ HR}}$  mixing ratio and  $[\text{OH}_{24\text{ HR}}]$  at 500 hPa (circle, Figures 8a, 8b, 8f, and 8g), even though this estimate is for October 2009 (later, we compare POLMIP output for October 2008 to these *Rex et al.* [2014] estimates). The OH profile for winter 2008 from the LMDZ-INCA CTM is in close agreement with OH from *Rex et al.* [2014] due to low  $\text{NO}_x$ ,  $\text{O}_3$ , and  $J(\text{O}^1\text{D})$  (Figures 8c, 9a, and 9c); all other CTMs calculate OH considerably higher than the *Rex et al.* [2014] value.

The comparison of OH precursors and related species from the POLMIP archive (winter 2008) to GV observations reveals similar tendencies as found for CAM-chem-SD (winter 2014, section 3.2) (Figures 8c–8e and 9a–9e). Observed mixing ratios of  $\text{NO}_x$  (Figure 8c) and HCHO (Figure 8d) between the surface and 500 hPa are much larger than found in any of the POLMIP CTMs, similar to the discrepancy between the GV observations and output of CAM-chem-SD (section 3.2). There is considerable spread in the profile of  $\text{O}_3$  among the CTMs

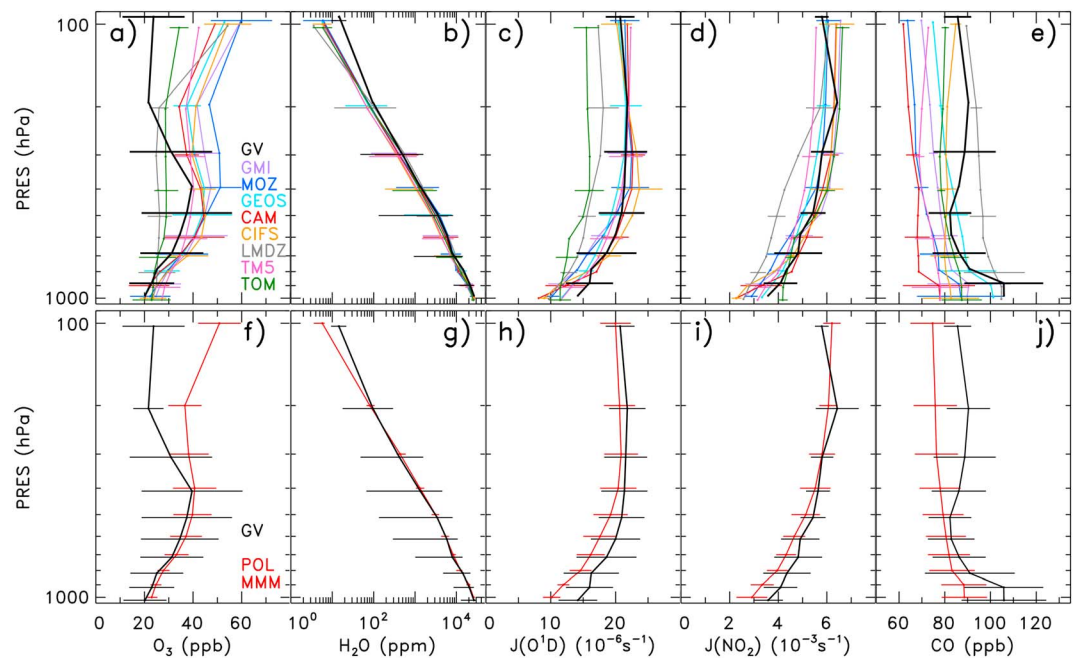


**Figure 9.** Same as Figure 8 except for (a, f)  $O_3$ , (b, g)  $H_2O$ , (c, h)  $J(O^1D)$ , (d, i)  $J(NO_2)$ , and (e, j)  $CO$  from observations and from the eight POLMIP CTMs. The comparisons for  $O_3$ ,  $H_2O$ , and  $CO$  show the monthly mean values from the POLMIP archive for January and February 2008 and the mean profiles observed during CONTRAST, since all of these quantities have long photochemical lifetimes. The plots for  $J(O^1D)$  and  $J(NO_2)$  compare monthly mean values from the POLMIP archive to 24 h averages of the diel output of  $J(O^1D)$  and  $J(NO_2)$  from DSMACC, for calculations constrained to match observed  $J(O^1D)$  and  $J(NO_2)$  at the SZA of observation. Error bars show 1 standard deviation about the mean, except for  $H_2O$ , where error bars represent the 5th and 95th percentiles.

(Figure 9a). For most of the troposphere the observed profile of  $O_3$  lies within the distribution of CTM profiles; however, between 100 and 200 hPa, observed  $O_3$  is consistently lower than all of the CTM values. The lowest values of  $O_3$  for much of the TWP troposphere are reported by LMDZ-INCA, which is consistent with the small values of OH from this CTM. Similarly, the observed profile of  $H_2O$  is within the range of CTM values for altitudes below  $\sim 200$  hPa (Figure 9b). Between 100 and 200 hPa, observed  $H_2O$  is consistently higher than all of the CTM values. These comparisons suggest that the mean state of  $O_3$  and  $H_2O$  in the TWP, from the surface to  $\sim 200$  hPa, is represented well within most of the POLMIP CTMs. The comparisons of  $O_3$  and  $H_2O$  between 100 and 200 hPa suggest a stronger influence of active convection (with  $O_3$ -deficient,  $H_2O$ -saturated air) in the TWP during January and February 2014 than simulated by the POLMIP CTMs for winter 2008.

We examine the effect of OH precursor differences between CONTRAST and the POLMIP CTMs by performing box model swap simulations, as were performed with CAM-chem-SD (described in section 2.3). The multimodel mean of each monthly OH precursor ( $O_3$ ,  $H_2O$ ,  $CO$ ,  $C_5H_8$ ,  $HCHO$ ,  $CH_3CHO$ ,  $NO_x$ ,  $J(O^1D)$ , and  $J(NO_2)$ ) are input individually to the DSMACC box model, which is otherwise constrained to GV observations. As in Figure 8j,  $C_5H_8$  is calculated as the median value within the POLMIP models rather than the mean. Scaling factors are applied to those species with significant diurnal variations. Since this configuration of the DSMACC box model requires constraints be specified at a specific local solar time, the monthly mean values of POLMIP  $HCHO$ ,  $NO_x$ ,  $J(O^1D)$ , and  $J(NO_2)$  have been scaled to represent values for local solar noon. Scaling factors for  $NO$ ,  $J(O^1D)$ , and  $J(NO_2)$  are derived from all GV box model runs for observations that occurred within 1 h of local solar noon and are calculated as  $[NO]_{INST}/[NO]_{24 HR}$ ,  $[J(O^1D)]_{INST}/[J(O^1D)]_{24 HR}$ , and  $[J(NO_2)]_{INST}/[J(NO_2)]_{24 HR}$ , respectively. All scaling factors are averaged within 100 hPa pressure bins and applied to the likewise pressure-binned POLMIP multimodel mean, for input to the box model. Because calculation of these scaling factors relies on the availability of GV observations that occurred close to noon, column integration is restricted to 1000 to 200 hPa (i.e., only this pressure range was sampled at enough times to allow empirical scaling factors to be found). Figures S10–12, respectively, show the  $NO$ ,  $J(O^1D)$ , and  $J(NO_2)$  scaling factors calculated by the box model as well as scaling factors

calculated from hourly output of the POLMIP CTMs, noted in the caption, that provided fields of each species. This latter comparison provides confidence that our method of scaling monthly mean concentrations to instantaneous noontime values is handled correctly.

The scaling factor for HCHO is calculated from the same output of the UWCM model used to generate 24 h average values of HCHO shown in Figures 8d and 8i. The same method is used to calculate the scaling factor,  $[\text{HCHO}]_{\text{INST}}/[\text{HCHO}]_{24 \text{ HR}}$ , but for all measurements that occurred within 2 h of solar noon, due to the coarser time resolution of the UWCM box model run. The HCHO scaling factor is shown in Figure S13.

The difference between the OH resulting from individual variable swaps and OH calculated from the baseline run of the DSMACC box model, constrained only to GV observations, Figure 10a, shows that  $\text{NO}_x$  is the dominant factor driving large negative differences in  $[\text{OH}_{24 \text{ HR}}]$  (negative indicates that the POLMIP precursor is responsible for a low value of CTM OH), particularly for pressures greater than  $\sim 400$  hPa. The highest values of observed  $\text{NO}_x$  in the midtroposphere during CONTRAST coincide with HOLW structures [Anderson *et al.*, 2016]. Figure 11c shows  $\text{NO}_x$  values calculated from observed NO and modeled steady state  $\text{NO}_2$ , separated by our categorization of HOLW and background conditions (section 2.6). Figures 11a and 11b show the bimodal distributions of  $\text{O}_3$  and  $\text{H}_2\text{O}$ , respectively, observed during CONTRAST. Previous work suggests that the source of these HOLW structures is biomass burning emissions from Africa and Southeast Asia [Anderson *et al.*, 2016]. It is interesting that the monthly mean values of both  $\text{O}_3$  and  $\text{H}_2\text{O}$  from POLMIP fall in between the extremes of the respective modes related to background conditions in the remote Pacific (solid black lines) and biomass burning structures (dotted black lines), whereas  $\text{NO}_x$  from most POLMIP CTMs lies close to that of the background TWP. Therefore, as noted in section 3.2, the underestimates of  $\text{NO}_x$  by the POLMIP CTMs is likely related to model treatment of nitrogen emissions, chemistry, and/or transport from distant landmasses.

Both  $J(\text{O}^1\text{D})$  and  $J(\text{NO}_2)$  contribute to the tendency for lower values of  $[\text{OH}_{24 \text{ HR}}]$  within POLMIP CTMs compared to GV OH, with  $J(\text{O}^1\text{D})$  driving the larger differences (Figure 10a). The most significant influence of  $J(\text{NO}_2)$  on  $[\text{OH}_{24 \text{ HR}}]$  occurs at low altitudes. As noted above, this finding results from the predominantly clear-sky sampling during CONTRAST. Ozone and  $\text{H}_2\text{O}$  from the POLMIP models also drive large differences in  $[\text{OH}_{24 \text{ HR}}]$ . The changes in  $[\text{OH}_{24 \text{ HR}}]$  derived from POLMIP  $\text{H}_2\text{O}$  fluctuate and are generally centered about zero, while those due to POLMIP  $\text{O}_3$  account for a high tendency in POLMIP OH. Indeed, multimodel mean  $\text{O}_3$  found for the POLMIP CTMs is higher than the mean  $\text{O}_3$  vertical profile from CONTRAST (Figure 9f), though the individual CTMs are either close to or spread about the observations except at the lowest pressures (Figure 9a). The tendency of POLMIP CTMs to overestimate observed  $\text{O}_3$  for pressures below 200 hPa could be indicative of convection within the models stopping at higher pressure (lower altitude) than in the actual TWP troposphere. Alternatively, the coarse vertical resolution of the models in the upper troposphere/lower stratosphere region could result in diffusion of more  $\text{O}_3$ -rich stratospheric air into the modeled upper troposphere than is realistic.

The OH precursors HCHO and  $\text{CH}_3\text{CHO}$  also influence  $[\text{OH}_{24 \text{ HR}}]$  (Figure 10a) in a manner similar to that seen for the CAM-chem-SD comparison. The use of HCHO from the POLMIP CTMs within the box model causes a decrease in  $[\text{OH}_{24 \text{ HR}}]$  at lower pressures ( $\leq \sim 200$  hPa), where HCHO is an important source of  $\text{HO}_x$  [Jaeglé *et al.*, 1998]. Conversely, constraining to the lower abundance of  $\text{CH}_3\text{CHO}$  from POLMIP causes an increase in OH near the ocean surface. As for CAM-chem-SD, oceanic emissions of  $\text{CH}_3\text{CHO}$  are absent from all POLMIP CTMs. This factor, possibly in combination with the other potential model misrepresentations of  $\text{CH}_3\text{CHO}$  production (section 3.1), results in an enormous gap between observed and modeled profiles of  $\text{CH}_3\text{CHO}$  (Figure 12). This comparison is shown using a linear scale (Figure 12a) to properly represent the difference between observed and modeled  $\text{CH}_3\text{CHO}$  and a logarithmic scale (Figure 12b) so that differences in  $\text{CH}_3\text{CHO}$  between the various POLMIP CTMs can be visualized. Since  $\text{CH}_3\text{CHO}$  is a sink for OH, the addition of an ocean source within CTMs will lower OH in the marine boundary layer [Read *et al.*, 2012].

Carbon monoxide exhibits a small effect on  $[\text{OH}_{24 \text{ HR}}]$  despite considerable differences in CO among the POLMIP models (Figure 9e) and the tendency of the POLMIP multimodel mean value of CO to be 10 to 15% lower than CONTRAST CO throughout the troposphere (Figure 9j). Many modeling studies have identified and sought to understand low biases in model CO [e.g., Shindell *et al.*, 2006; Mao *et al.*, 2013b; Naik *et al.*, 2013; Monks *et al.*, 2015; Strode *et al.*, 2015], with explanations ranging from underestimated CO from fossil fuel and biomass burning in emissions inventories [Shindell *et al.*, 2006] to overestimated OH (the main sink

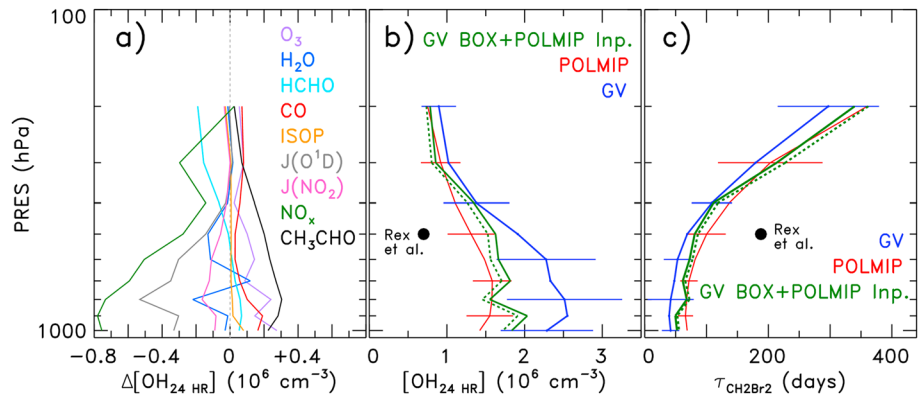


**Figure 10.** (a) The difference in  $[OH_{24 HR}]$  between a run of the DSMACC box model constrained to GV observations of all OH precursors with the exception of the indicated species and another run of the model constrained to GV observations of all OH precursors, where indicated species refers to the POLMIP multimodel mean value. These box model difference plots have been conducted at 100 hPa intervals. (b) The mean and standard deviation  $[OH_{24 HR}]$  profile calculated by the DSMACC box model constrained to GV observations of OH precursors (blue) compared to the multimodel mean and standard deviation of monthly mean  $[OH]$  in the POLMIP archive from eight CTMs (red). The solid green line represents  $[OH_{24 HR}]^{CONTRAST} + \Delta[OH_{24 HR}]^{ALL}$ , where  $\Delta[OH_{24 HR}]^{ALL}$  represents the difference between a run of the DSMACC box model constrained to POLMIP multimodel mean values of all nine OH precursors and another run of the model constrained to GV observations of all nine OH precursors. The profile of  $\Delta[OH_{24 HR}]^{ALL}$  is nearly identical to the sum of the nine terms shown in Figure 10a (see supporting information). The dashed green line is adjusted to account for the 13% high bias in daytime OH calculated by the box model, or ~6.5% high bias in  $OH_{24 HR}$ , attributable to the box model chemical mechanism (from Figure 5d). The calculation of the dashed green line is identical to the solid green line except that values of  $[OH_{24 HR}]$  are multiplied by  $1/1.065$ . (c) Lifetime of  $CH_2Br_2$  ( $\tau_{CH_2Br_2}$ ) with respect to loss by OH for  $[OH_{24 HR}]$  from the box model constrained to GV measurements (blue), for the multimodel monthly mean  $[OH]$  from the POLMIP CTMs (red), and for  $[OH_{24 HR}]$  from the box model constrained to the nine OH precursors from POLMIP (solid green). The dashed green line in Figure 10c shows  $\tau_{CH_2Br_2}$  calculated for adjusted values of  $[OH_{24 HR}]$  in Figure 10b represented by the green dashed line. Values of  $[OH_{24 HR}]$  and  $\tau_{CH_2Br_2}$  reported by Rex *et al.* [2014] at 500 hPa for October 2009 in the TWP are shown in Figures 10b and 10c.

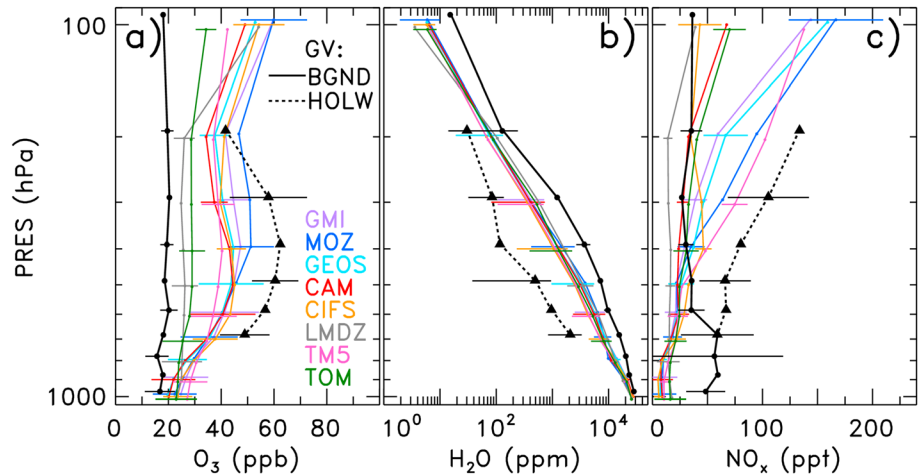


**Figure 11.** Vertical profiles of monthly mean (a)  $O_3$ , (b)  $H_2O$ , and (c)  $NO_x$  mixing ratio from the POLMIP archive for eight CTMs (colored lines) for January and February 2008 compared to profiles of these three species measured by the GV during CONTRAST for background conditions (BGND) and well-defined high  $O_3$ , low  $H_2O$  (HOLW) structures. Criteria for BGND are simultaneous  $RH > 70\%$ ,  $O_3 < 25$  ppb; criteria for HOLW are simultaneous  $RH < 20\%$ ,  $O_3 > 40$  ppb. Relative humidity (RH) is calculated from observed  $H_2O$  and temperature ( $T$ ), with respect to liquid water for  $T > 0^\circ C$  and with respect to ice for  $T < 0^\circ C$ . The GV profiles of  $NO_x$  are the sum of measured  $NO$  and box modeled  $NO_2$  at the time of observation. Since we are showing GV profiles obtained only during daylight conditions, the POLMIP  $NO_x$  profile (archived as monthly mean) has been scaled by the mean profile of  $([NO_{INST}] + [NO_2_{INST}]) / ([NO_{24 HR}] + [NO_{24 HR}])$  calculated from the box model simulations of the GV data. A profile of this ratio, which is close to unity, is shown in the supporting information. Error bars represent 1 standard deviation about the mean for 100 hPa pressure bins; they are offset slightly in the vertical for clarity. Some of the error bars are omitted to avoid clutter.

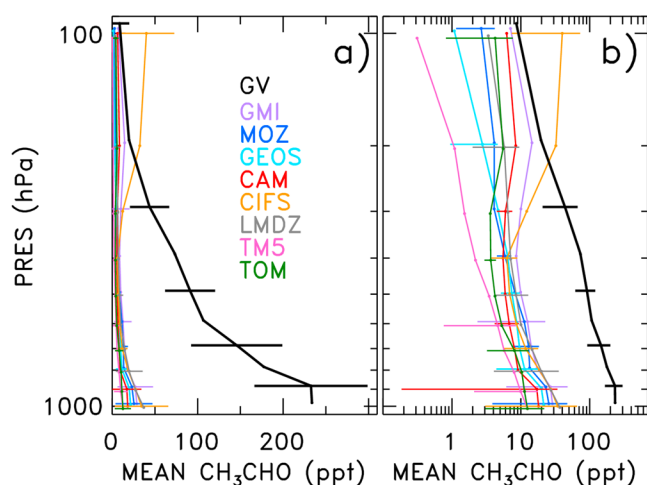


**Figure 12.** Same as Figure 8 except only showing monthly mean  $\text{CH}_3\text{CHO}$  values from individual POLMIP CTMs (colors) and from CONTRAST campaign (black) using (a) a linear scale and (b) a log scale.

for CO) in the Northern Hemisphere [Strode *et al.*, 2015]. Whatever the cause, underestimation of the CO sink in the POLMIP CTMs leads to a small positive perturbation in  $[\text{OH}_{24 \text{ HR}}]$ , much less in magnitude than the perturbations due to  $\text{NO}_x$ ,  $J(\text{O}^1\text{D})$ , and  $\text{CH}_3\text{CHO}$ .

Finally,  $\text{C}_5\text{H}_8$  drives near-zero differences in  $[\text{OH}_{24 \text{ HR}}]$  throughout the troposphere. Isoprene in the midtroposphere to upper troposphere, at pressures lower than  $\sim 800$  hPa, was almost always below the detection limit of the TOGA instrument (1 ppt). This is not surprising, given the remote region of the observations and the short lifetime of  $\text{C}_5\text{H}_8$ .

One additional box model simulation is performed in which all nine POLMIP OH precursors ( $\text{O}_3$ ,  $\text{H}_2\text{O}$ , CO,  $\text{C}_5\text{H}_8$ , HCHO,  $\text{CH}_3\text{CHO}$ ,  $\text{NO}_x$ ,  $J(\text{O}^1\text{D})$ , and  $J(\text{NO}_2)$ ) are simultaneously used as constraints. The difference in  $[\text{OH}_{24 \text{ HR}}]$  between the baseline run of the box model, constrained only to CONTRAST observations of the precursors, and this simulation ( $\Delta[\text{OH}_{24 \text{ HR}}]$ ) is nearly identical to the sum of the  $[\text{OH}_{24 \text{ HR}}]$  differences due to each species from Figure 10a (Figure S14). The total  $\Delta[\text{OH}_{24 \text{ HR}}]$  is added to the campaign-wide  $[\text{OH}_{24 \text{ HR}}]$  vertical profile to determine whether these nine factors describe the difference between GV and POLMIP OH. The result of this analysis (solid green line, Figure 10b) generally matches the OH from the POLMIP MMM (red line) in the upper troposphere, though values in the low to midtroposphere overestimate those from POLMIP. Subsequently,  $\tau_{\text{CH}_2\text{Br}_2}$  derived from these  $[\text{OH}_{24 \text{ HR}}]$  values shows that switching to box model constraint of the nine POLMIP OH precursors matches the POLMIP  $\tau_{\text{CH}_2\text{Br}_2}$  values in the upper troposphere (solid green line, Figure 10c) but underestimates  $\tau_{\text{CH}_2\text{Br}_2}$  in the lower and midtroposphere. However, recall from section 3.2 that the box model chemical mechanism could contribute a difference in calculated  $[\text{OH}_{24 \text{ HR}}]$  as high as 6.5%. When adjusted to account for this difference, our simulations agree quite well with values of  $[\text{OH}_{24 \text{ HR}}]$  and  $\tau_{\text{CH}_2\text{Br}_2}$  from the POLMIP MMM (dashed green lines, Figures 10b and 10c). We infer from this result that the offset in OH driven by the box model chemical mechanism is consistent when compared to both CAM-chem-SD and the POLMIP suite of CTMs.

We also tabulate quantitative analysis of  $\text{OH}^{\text{COL}}$  values modeled by replacing, individually, GV observations of OH precursors with POLMIP multimodel mean (MMM) values. Values of  $\text{OH}^{\text{COL}}$  for each simulation are shown in Table 2. Overall, the GV-based value of  $\text{OH}^{\text{COL}}$  is 41% larger than the POLMIP MMM value  $\text{OH}^{\text{COL}}$ . The analysis shows that use of  $\text{NO}_x$  from observations results in a 28% increase in  $\text{OH}^{\text{COL}}$ , due to the increase in secondary production of OH. Observed fields of  $J(\text{O}^1\text{D})$  and  $J(\text{NO}_2)$  result in 11% and 4% increases, respectively, in  $\text{OH}^{\text{COL}}$  relative to the POLMIP  $\text{OH}^{\text{COL}}$ . This supports the conclusion that primarily clear-sky sampling during CONTRAST leads to a  $\sim 15\%$  overestimate of  $\text{OH}^{\text{COL}}$ . Acetaldehyde is the next important individual precursor; the use of the observed profile results in a 9% underestimate of  $\text{OH}^{\text{COL}}$ , since the observed concentrations of  $\text{CH}_3\text{CHO}$  act as a fairly strong OH sink. All of the other precursors make minor contributions to the difference between GV and POLMIP  $\text{OH}^{\text{COL}}$ . If we attribute 15% of the 41% difference in these two quantities to the clear-sky sampling bias of CONTRAST, and another 6.5% to the tendency of the DSMACC chemical mechanism to overestimate OH relative to the mechanisms within global models, then we conclude that precursor conditions in the TWP observed during January and February 2014 led to  $\text{OH}^{\text{COL}}$  being  $\sim 20\%$  larger than the POLMIP MMM value for January and February 2008.

Finally, we use the POLMIP archive to determine the extent to which seasonal differences in OH precursors could explain the difference between inferred OH from the CONTRAST campaign and from Rex *et al.* [2014]. We compare values of  $\text{OH}_{24 \text{ HR}}$  calculated for the CONTRAST campaign for January–February 2014,

**Table 2.** Tropospheric OH Columns Calculated for the CONTRAST Mean OH Vertical Profile and POLMIP Model Simulations

POLMIP Box Model Run	OH Column <sup>a</sup> ( $10^{12} \text{ cm}^{-2}$ )	Ratio (GV/Run X)
GV	2.17	---
POLMIP MMM	1.54	1.41
GV, POL NO <sub>x</sub>	1.70	1.28
GV, POL J(O <sup>1</sup> D)	1.96	1.11
GV, POL CH <sub>3</sub> CHO	2.38	0.91
GV, POL O <sub>3</sub>	2.30	0.94
GV, POL CO	2.26	0.96
GV, POL J(NO <sub>2</sub> )	2.09	1.04
GV, POL HCHO	2.11	1.03
GV, POL H <sub>2</sub> O	2.12	1.02
GV, POL C <sub>5</sub> H <sub>8</sub>	2.17	1.00

<sup>a</sup>Columns are integrated from the surface to 200 hPa (~13 km).

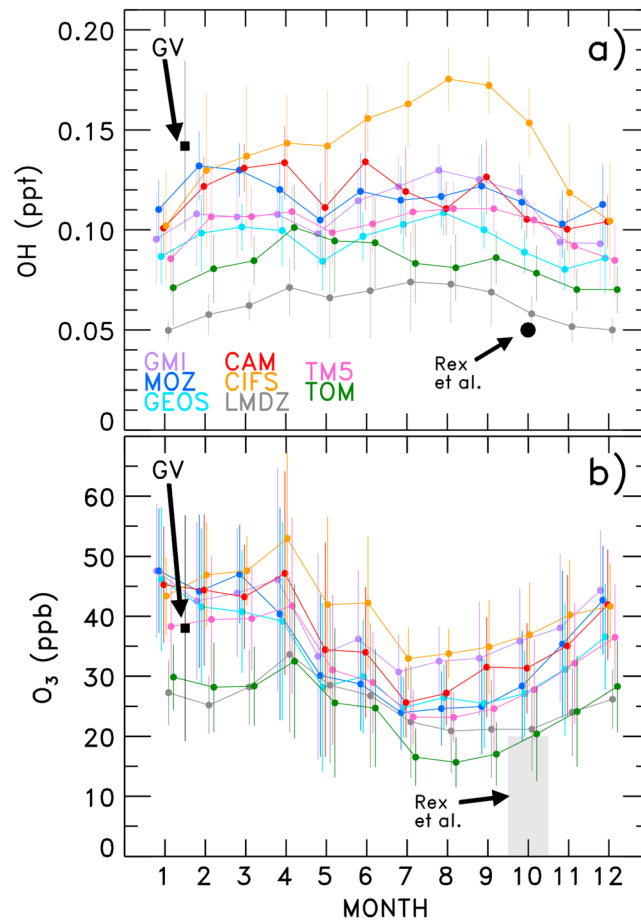


**Figure 13.** Seasonal variation of monthly mean (a) OH mixing ratio and (b) O<sub>3</sub> mixing ratio from the eight POLMIP CTMs, for the pressure level closest to 500 hPa. The black squares show the mean and standard deviation of OH<sub>24 HR</sub> (Figure 13a) and O<sub>3</sub> (Figure 13b) inferred from the CONTRAST GV observations, both at 500 ± 50 hPa. The black circle shows OH<sub>24 HR</sub> (Figure 13a) at 500 hPa for October 2009 from *Rex et al.* [2014]. The grey box in Figure 13b shows the range of O<sub>3</sub> reported by *Rex et al.* [2014] in the TWP at 500 hPa for October 2009.

OH<sub>24 HR</sub> simulated by GEOS-Chem in *Rex et al.* [2014] for October 2009, and monthly mean OH mixing ratios simulated by the POLMIP models for each month in 2008, all at 500 hPa (Figure 13). At this pressure level, for the corresponding months, no POLMIP model simulates mean TWP OH<sub>24 HR</sub> as high as our estimate, nor does any model simulate a mean OH<sub>24 HR</sub> as low as the *Rex et al.* [2014] value. None of the POLMIP CTMs exhibit seasonal variation in OH or O<sub>3</sub> anywhere close to that which would be necessary to explain both the GV and *Rex et al.* [2014] based values. Both the box model-based estimate of OH<sub>24 HR</sub> and the *Rex et al.* [2014] CTM-based estimate of OH<sub>24 HR</sub> are grounded in observations of O<sub>3</sub> (along with other chemical species and radiative variables, for our estimate). As discussed in section 3.2, the ozonesonde data collected during the TransBrom cruise in *Rex et al.* [2014] may exhibit a low bias as a result of calibration technique [*Newton et al.*, 2016]; their reported O<sub>3</sub> mixing ratios often fell below 15 ppb as indicated by the shaded region in Figure 13b. None of the POLMIP CTMs produce values of O<sub>3</sub> as low as those reported by *Rex et al.* [2014]. On the other hand, the campaign-wide mixing ratio of O<sub>3</sub> at 500 hPa from CONTRAST lies in the middle of the range of O<sub>3</sub> from the POLMIP CTMs.

Interannual variations in tropospheric composition may play a role in explaining the large discrepancy in OH<sub>24 HR</sub> reported here compared to that of *Rex et al.* [2014]. Biomass burning differences between the *Rex et al.* [2014] study period (October 2009) and that of CONTRAST (January/February 2014) are large (Figures S1a and S1c). The number of fires per month in Africa, north of the equator, for October 2009 is only ~8% of that observed by MODIS for January/February 2014. This difference is a result of seasonal shifts in the location of biomass

burning. This shift should, however, be represented within the POLMIP CTMs (albeit, for 1 year after the *Rex et al.* [2014] cruise). Differences in the ENSO conditions between 2008 and 2014 must also be considered. The Multivariate ENSO Index for CONTRAST during January/February 2014 was neutral, whereas the *Rex et al.* [2014] study took place during a moderately strong El Niño event at the end of 2009 [Wolter and Timlin, 2011]. The expected ENSO-induced changes in O<sub>3</sub> are counter to what we would expect to explain this discrepancy. Suppressed convection in the TWP during an El Niño event would enable O<sub>3</sub> to build to higher concentrations than normal [Ziemke et al., 2010]. Furthermore, increased stratosphere-to-troposphere exchange following an El Niño event should increase O<sub>3</sub> in the upper troposphere [Zeng and Pyle, 2005]. However, *Rex et al.* [2014] observed much lower O<sub>3</sub> during October 2009 than we observed during the neutral ENSO conditions in 2014. Hence, interannual effects most commonly associated with tropospheric composition do not readily explain the differences in observed O<sub>3</sub> and calculated OH<sub>24 HR</sub> between *Rex et al.* [2014] and this study.

#### 4. Conclusions

Box model calculations of OH were performed for the CONTRAST campaign that occurred in the TWP during January–February 2014 using the NSF/NCAR GV aircraft. The DSMACC box model was constrained to measurements of O<sub>3</sub>, CO, NO, HCHO, H<sub>2</sub>O, C<sub>3</sub>H<sub>8</sub>, CH<sub>4</sub>, C<sub>5</sub>H<sub>8</sub>, CH<sub>3</sub>COCH<sub>3</sub>, CH<sub>3</sub>OH, CH<sub>3</sub>CHO, J(O<sup>1</sup>D), and J(NO<sub>2</sub>). Comparisons and additional box model simulations were conducted to understand the differences between the measurement-inferred GV OH and OH from CAM-chem-SD and POLMIP CTM simulations.

We find that OH<sup>COL</sup> calculated by the CAM-chem-SD model using 2014 meteorology agrees remarkably well—to within 1%—with OH<sup>COL</sup> inferred from the GV observations after accounting for the tendency to sample clear-sky conditions during the CONTRAST campaign. However, compensating factors lead to this good agreement. A 26% low bias in CAM-chem-SD OH<sup>COL</sup> results from underestimates in NO<sub>x</sub> throughout the troposphere, relative to observations. Additionally, CAM-chem-SD overestimates OH<sup>COL</sup> by 10% due to underestimated CH<sub>3</sub>CHO in the lower troposphere, overestimates OH<sup>COL</sup> by 6% due to underestimated CO throughout the troposphere, and underestimates OH<sup>COL</sup> by 4% due to underestimated HCHO. Variations in OH<sup>COL</sup> due to O<sub>3</sub> and H<sub>2</sub>O arise from differences in the precise geographical location of high O<sub>3</sub>/low H<sub>2</sub>O (HOLW) structures [Pan et al., 2015; Anderson et al., 2016], which cannot be perfectly reproduced by global models.

An analysis of chemical fields within the POLMIP CTM archive (using 2008 meteorology) [Emmons et al., 2015] and GV OH revealed that observationally based GV OH<sup>COL</sup> was 40% larger than the POLMIP multimodel mean. About 15% of this difference was attributed to a clear-sky sampling bias of the CONTRAST GV, and another 6.5% may be due to the tendency of the DSMACC chemical mechanism to report higher levels of OH than found within CAM-chem-SD. As a result, differences in precursor fields lead to GV OH<sup>COL</sup> being ~20% larger than the POLMIP multimodel mean value. As with the CAM-chem-SD analysis, NO<sub>x</sub> is the single most important precursor field for OH. Observed NO<sub>x</sub> was nearly a factor of 2 larger than found within POLMIP CTMs for the middle and lower troposphere, resulting in higher levels of OH when constrained to GV observations due to secondary production of OH. All of the POLMIP CTMs severely underestimate the observed profile of acetaldehyde (CH<sub>3</sub>CHO), due either to the neglect of ocean emission of this compound or a misrepresentation of either primary or secondary atmospheric production. Consistent with the analysis of tropical ground-based observations from Cape Verde [Read et al., 2012], we show that the improvement of model representation of CH<sub>3</sub>CHO will likely suppress OH in the lower troposphere, due to the highly reactive nature of this compound.

We find no evidence for suppressed levels of OH in the TWP. Mean values of [OH<sub>24 HR</sub>] remain above  $2 \times 10^6 \text{ cm}^{-3}$  (mixing ratio of ~0.1 ppt) throughout the TWP troposphere. Our measurements of O<sub>3</sub> reached a minimum of ~20 ppb, and as a result, the primary production of HO<sub>x</sub> was not anomalously low in the TWP. A possible explanation for the marked difference in [OH<sub>24 HR</sub>] at the 500 hPa level of the TWP reported here and that given by *Rex et al.* [2014] is that the O<sub>3</sub> mixing ratio minimum of *Rex et al.* [2014] was biased low, due to their ozonesonde calibration procedure [Newton et al., 2016]. Finally, the extremely low concentrations of NO tied to the TWP by *Gao et al.* [2014] were rarely observed during CONTRAST. Rather, the abundance of NO<sub>x</sub> inferred from CONTRAST NO was more than a factor of 2 higher than found within either CAM-chem-SD or the POLMIP CTMs, perhaps due to improper representation of outflow from regions of active biomass

burning [Anderson *et al.*, 2016] in these global models. The high levels of NO observed in the tropical troposphere during CONTRAST sustain larger values of OH than found within global models, due to the recycling of HO<sub>2</sub>.

While this new observationally constrained estimate of OH may help global models that run active chemistry evaluate their simulations of OH, it should be noted that our study does not resolve a present dilemma regarding the oxidative capacity of the troposphere. The majority of global models calculate values of  $\tau_{\text{CH}_4}$  about 1.75 years smaller [Naik *et al.*, 2013] than the current best empirical estimate of  $\tau_{\text{CH}_4}$  ( $11.2 \pm 1.3$  years, due to loss by reaction with tropospheric OH only) [Prather *et al.*, 2012]. If our finding that [OH] within global models is too low due to an underestimate of observed NO<sub>x</sub> happens to hold for other regions of the tropics, then the discrepancy between  $\tau_{\text{CH}_4}$  found by global models and that inferred from measurements of CH<sub>3</sub>CCl<sub>3</sub> could grow. However, our results are representative of a small region of the globe. While they are positioned within the crucial tropical band, they may not be representative of global model calculations of OH. The planned airborne measurements of OH, NO<sub>x</sub>, NO<sub>y</sub>, H<sub>2</sub>O, CH<sub>4</sub>, O<sub>3</sub>, HCHO, actinic flux, and many other species of interest by the upcoming NASA Atmospheric Tomography Mission (ATom) over numerous tropical oceanic regions [NOAA, 2014] will shed important new light on the oxidative capacity of the tropical troposphere.

#### Acknowledgments

We thank T. Robinson and O. Shieh for providing meteorology forecasts in the field and the pilots and crew of the CONTRAST Gulfstream V aircraft for their dedication and professionalism. We thank the three anonymous reviewers for their constructive comments that improved this manuscript. CONTRAST was funded by the National Science Foundation. We would like to acknowledge high-performance computing support from Yellowstone (ark:/85065/d7wd3xhc) provided by NCAR's Computational and Information Systems Laboratory. The National Center for Atmospheric Research is sponsored by the National Science Foundation. Work conducted at the University of Maryland was supported, in part, by the NASA Modeling and Analysis Program. G.M.W., D.C.A., and T.F.H. received support for the NASA Upper Atmospheric Research Program under NNN12ZDA001N-UACO. JM acknowledges support from the NOAA Climate Program Office grant NA13OAR4310071. CONTRAST data are publicly available for all researchers and can be obtained at [http://data.eol.ucar.edu/master\\_list/?project=CONTRAST](http://data.eol.ucar.edu/master_list/?project=CONTRAST). The CAM-Chem-SD and POLMIP model simulations are available upon request to the authors (julie.m.nicely@nasa.gov).

#### References

- Anderson, D., *et al.* (2016), A pervasive role for biomass burning in tropical high ozone/low water structures, *Nat. Commun.*, *7*, doi:10.1038/ncomms10267.
- Apel, E. C., *et al.* (2015), Upper tropospheric ozone production from lightning NO<sub>x</sub>-impacted convection: Smoke ingestion case study from the DC3 campaign, *J. Geophys. Res. Atmos.*, *120*, 2505–2523, doi:10.1002/2014JD022121.
- Aschmann, J., B. M. Sinnhuber, E. L. Atlas, and S. M. Schauffler (2009), Modeling the transport of very short-lived substances into the tropical upper troposphere and lower stratosphere, *Atmos. Chem. Phys.*, *9*(23), 9237–9247, doi:10.5194/acp-9-9237-2009.
- Ashfold, M. J., N. R. P. Harris, E. L. Atlas, A. J. Manning, and J. A. Pyle (2012), Transport of short-lived species into the Tropical Tropopause Layer, *Atmos. Chem. Phys.*, *12*(14), 6309–6322, doi:10.5194/acp-12-6309-2012.
- Bey, I., D. J. Jacob, R. M. Yantosca, J. A. Logan, B. D. Field, A. M. Fiore, Q. Li, H. Y. Liu, L. J. Mickley, and M. G. Schultz (2001), Global modeling of tropospheric chemistry with assimilated meteorology: Model description and evaluation, *J. Geophys. Res.*, *106*, 23,073–23,095, doi:10.1029/2001JD000807.
- Bloss, W. J., M. J. Evans, R. Sommariva, D. E. Heard, and M. J. Pilling (2005), The oxidative capacity of the troposphere: Coupling of field measurements of OH and a global chemistry transport model, *Faraday Discuss.*, *130*, 425–436, doi:10.1039/B419090D.
- Brune, W. H., *et al.* (1998), Airborne in-situ OH and HO<sub>2</sub> observations in the cloud-free troposphere and lower stratosphere during SUCCESS, *Geophys. Res. Lett.*, *25*, 1701–1704, doi:10.1029/97GL03098.
- Calvert, J. G., F. Su, J. W. Bottenheim, and O. P. Strausz (1978), Mechanism of homogeneous oxidation of sulfur-dioxide in troposphere, *Atmos. Environ.*, *12*(1–3), 197–226, doi:10.1016/0004-6981(78)90201-9.
- Cazorla, M., G. M. Wolfe, S. A. Bailey, A. K. Swanson, H. L. Arkinson, and T. F. Hanisco (2015), A new airborne laser-induced fluorescence instrument for in situ detection of formaldehyde throughout the troposphere and lower stratosphere, *Atmos. Meas. Tech.*, *8*(2), 541–552, doi:10.5194/amt-8-541-2015.
- Chipperfield, M. P. (2006), New version of the TOMCAT/SLIMCAT off-line chemical transport model: Intercomparison of stratospheric tracer experiments, *Q. J. R. Meteorol. Soc.*, *132*, 1179–1203, doi:10.1256/qj.05.51.
- Crawford, J. H., *et al.* (1997), Implications of large scale shifts in tropospheric NO<sub>x</sub> levels in the remote tropical Pacific, *J. Geophys. Res.*, *102*, 28,447–28,468, doi:10.1029/97JD00011.
- Crosson, E. R. (2008), A cavity ring-down analyzer for measuring atmospheric levels of methane, carbon dioxide, and water vapor, *Appl. Phys. B-Lasers O.*, *92*(3), 403–408, doi:10.1007/s00340-008-3135-y.
- Damian, V., A. Sandu, M. Damian, F. Potra, and G. R. Carmichael (2002), The Kinetic PreProcessor KPP—A software environment for solving chemical kinetics, *Comput. Chem. Eng.*, *26*(11), 1567–1579, doi:10.1016/S0098-1354(02)00128-X.
- Duncan, B. N., S. E. Strahan, Y. Yoshida, S. D. Steenrod, and N. Livesey (2007), Model study of the cross-tropopause transport of biomass burning pollution, *Atmos. Chem. Phys.*, *7*, 3713–3736, doi:10.5194/acp-7-3713-2007.
- Eisele, F. L., D. J. Tanner, C. A. Cantrell, and J. G. Calvert (1996), Measurements and steady state calculations of OH concentrations at Mauna Loa Observatory, *J. Geophys. Res.*, *101*, 14,665–14,679, doi:10.1029/95JD03654.
- Emmerson, K. M., and M. J. Evans (2009), Comparison of tropospheric gas-phase chemistry schemes for use within global models, *Atmos. Chem. Phys.*, *9*(5), 1831–1845, doi:10.5194/acp-9-1831-2009.
- Emmons, L. K., *et al.* (2010), Description and evaluation of the Model for Ozone and Related chemical Tracers, version 4 (MOZART-4), *Geosci. Model Dev.*, *3*, 43–67, doi:10.5194/gmd-3-43-2010.
- Emmons, L. K., *et al.* (2015), The POLARCAT Model Intercomparison Project (POLMIP): Overview and evaluation with observations, *Atmos. Chem. Phys.*, *15*(12), 6721–6744, doi:10.5194/acp-15-6721-2015.
- Fernandez, R. P., R. J. Salawitch, D. E. Kinnison, J.-F. Lamarque, and A. Saiz-Lopez (2014), Bromine partitioning in the tropical tropopause layer: Implications for stratospheric injection, *Atmos. Chem. Phys.*, *14*(24), 13,391–13,410, doi:10.5194/acp-14-13391-2014.
- Fiore, A. M., *et al.* (2009), Multimodel estimates of intercontinental source-receptor relationships for ozone pollution, *J. Geophys. Res.*, *114*, D04301, doi:10.1029/2008JD010816.
- Flemming, J., *et al.* (2015), Tropospheric chemistry in the Integrated Forecasting System of ECMWF, *Geosci. Model Dev.*, *8*, 975–1003, doi:10.5194/gmd-8-975-2015.
- Fueglistaler, S., H. Wernli, and T. Peter (2004), Tropical troposphere-to-stratosphere transport inferred from trajectory calculations, *J. Geophys. Res.*, *109*, D03108, doi:10.1029/2003JD004069.
- Gao, R. S., K. H. Rosenlof, D. W. Fahey, P. O. Wennberg, E. J. Hints, and T. F. Hanisco (2014), OH in the tropical upper troposphere and its relationships to solar radiation and reactive nitrogen, *J. Atmos. Chem.*, *71*(1), 55–64, doi:10.1007/s10874-014-9280-2.

- Gerbig, C., S. Schmitgen, D. Kley, A. Volz-Thomas, K. Dewey, and D. Haaks (1999), An improved fast-response vacuum-UV resonance fluorescence CO instrument, *J. Geophys. Res.*, *104*, 1699–1704, doi:10.1029/1998JD100031.
- Hatsushika, H., and K. Yamazaki (2003), Stratospheric drain over Indonesia and dehydration within the tropical tropopause layer diagnosed by air parcel trajectories, *J. Geophys. Res.*, *108*(D19), 4610, doi:10.1029/2002JD002986.
- Hauglustaine, D. A., F. Hourdin, L. Jourdain, M.-A. Filiberti, S. Walters, J.-F. Lamarque, and E. A. Holland (2004), Interactive chemistry in the Laboratoire de Météorologie Dynamique general circulation model: Description and background tropospheric chemistry evaluation, *J. Geophys. Res.*, *109*, D04314, doi:10.1029/2003JD003957.
- Hauglustaine, D. A., J. Lathiere, S. Szopa, and G. A. Folberth (2005), Future tropospheric ozone simulated with a climate-chemistry-biosphere model, *Geophys. Res. Lett.*, *32*, L24807, doi:10.1029/2005GL024031.
- Hoell, J. M., D. D. Davis, S. C. Liu, R. Newell, M. Shipham, H. Akimoto, R. J. McNeal, R. J. Bendura, and J. W. Drewry (1996), Pacific Exploratory Mission-West A (PEM-West A): September–October 1991, *J. Geophys. Res.*, *101*, 1641–1653, doi:10.1029/95JD00622.
- Hoell, J. M., D. D. Davis, S. C. Liu, R. Newell, H. Akimoto, R. J. McNeal, and R. J. Bendura (1997), The Pacific Exploratory Mission-West Phase B: February–March, 1994, *J. Geophys. Res.*, *102*, 28,223–28,239, doi:10.1029/97JD02581.
- Hossaini, R., M. P. Chipperfield, W. Feng, T. J. Breider, E. Atlas, S. A. Montzka, B. R. Miller, F. Moore, and J. Elkins (2012), The contribution of natural and anthropogenic very short-lived species to stratospheric bromine, *Atmos. Chem. Phys.*, *12*(1), 371–380, doi:10.5194/acp-12-371-2012.
- Hough, A. M., and R. G. Derwent (1987), Computer modeling studies of the distribution of photochemical ozone production between different hydrocarbons, *Atmos. Environ.*, *21*(9), 2015–2033, doi:10.1016/0004-6981(87)90163-6.
- Houghton, J. T., et al. (Eds.) (1996), Climate Change 1995, in *The Science of Climate Change*, 572 pp., Cambridge Univ. Press, U. K.
- Hourdin, F., et al. (2006), The LMDZ4 general circulation model: Climate performance and sensitivity to parametrized physics with emphasis on tropical convection, *Clim. Dynam.*, *27*, 787–813, doi:10.1007/s00382-006-0158-0.
- Huijnen, V., et al. (2010), The global chemistry transport model TM5: Description and evaluation of the tropospheric chemistry version 3.0, *Geosci. Model Dev.*, *3*, 445–473, doi:10.5194/gmd-3-445-2010.
- Intergovernmental Panel on Climate Change (2013), Climate Change 2013: The Physical Science Basis, in *Contribution of Working Group I to the Fifth Assessment Report of the Intergovernmental Panel on Climate Change*, 1535 pp., Cambridge Univ. Press, Cambridge, U. K., and New York.
- Jacob, D. J., et al. (1996), Origin of ozone and NO<sub>x</sub> in the tropical troposphere: A photochemical analysis of aircraft observations over the South Atlantic basin, *J. Geophys. Res.*, *101*, 24,235–24,250, doi:10.1029/96JD00336.
- Jacob, D. J., J. H. Crawford, M. M. Kleb, V. S. Connors, R. J. Bendura, J. L. Raper, G. W. Sachse, J. C. Gille, L. Emmons, and C. L. Heald (2003), Transport and Chemical Evolution over the Pacific (TRACE-P) aircraft mission: Design, execution, and first results, *J. Geophys. Res.*, *108*(D20), 9000, doi:10.1029/2002JD003276.
- Jaeglé, L., D. J. Jacob, W. H. Brune, D. Tan, I. C. Faloon, A. J. Weinheimer, B. A. Ridley, T. L. Campos, and G. W. Sachse (1998), Sources of HO<sub>x</sub> and production of ozone in the upper troposphere over the United States, *Geophys. Res. Lett.*, *25*, 1709–1712, doi:10.1029/98GL00041.
- Jenkin, M. E., S. M. Saunders, and M. J. Pilling (1997), The tropospheric degradation of volatile organic compounds: A protocol for mechanism development, *Atmos. Environ.*, *31*(1), 81–104, doi:10.1016/s1352-2310(96)00105-7.
- Jenkin, M. E., J. C. Young, and A. R. Rickard (2015), The MCM v3.3 degradation scheme for isoprene, *Atmos. Chem. Phys. Discuss.*, *15*(6), 9709–9766, doi:10.5194/acpd-15-9709-2015.
- Johnson, C. E., W. J. Collins, D. S. Stevenson, and R. G. Derwent (1999), Relative roles of climate and emissions changes on future tropospheric oxidant concentrations, *J. Geophys. Res.*, *104*, 18,631–18,645, doi:10.1029/1999JD900204.
- Krol, M., and J. Lelieveld (2003), Can the variability in tropospheric OH be deduced from measurements of 1,1,1-trichloroethane (methyl chloroform)?, *J. Geophys. Res.*, *108*(D3), 4125, doi:10.1029/2002JD002423.
- Kruger, K., and B. Quack (2013), Introduction to special issue: The TransBrom Sonne expedition in the tropical West Pacific, *Atmos. Chem. Phys.*, *13*(18), 9439–9446, doi:10.5194/acp-13-9439-2013.
- Lamarque, J.-F., et al. (2012), CAM-chem: Description and evaluation of interactive atmospheric chemistry in the Community Earth System Model, *Geosci. Model Dev.*, *5*(2), 369–411, doi:10.5194/gmd-5-369-2012.
- Law, K., et al. (2014), Arctic air pollution: New insights from POLARCAT-IPY, *Bull. Am. Meteorol. Soc.*, *95*(12), 1873–1895, doi:10.1175/BAMS-D-13-00017.1.
- Law, K. S., et al. (2007), Halogenated very short-lived substances, in *Scientific Assessment of Ozone Depletion: 2006, Global Ozone Res. and Monitoring Proj.—Rep. 50*, Chap. 2, pp. 572, World Meteorol. Org., Geneva, Switz.
- Levy, H. (1971), Normal atmosphere: Large radical and formaldehyde concentrations predicted, *Science*, *173*(3992), 141–143, doi:10.1126/science.173.3992.141.
- Liang, Q., E. Atlas, D. Blake, M. Dorf, K. Pfeilsticker, and S. Schaufli (2014), Convective transport of very short lived bromocarbons to the stratosphere, *Atmos. Chem. Phys.*, *14*(11), 5781–5792, doi:10.5194/acp-14-5781-2014.
- Mao, J., et al. (2010), Chemistry of hydrogen oxide radicals (HO<sub>x</sub>) in the Arctic troposphere in spring, *Atmos. Chem. Phys.*, *10*(13), 5823–5838, doi:10.5194/acp-10-5823-2010.
- Mao, J., F. Paulot, D. J. Jacob, R. C. Cohen, J. D. Crounse, P. O. Wennberg, C. A. Keller, R. C. Hudman, M. P. Barkley, and L. W. Horowitz (2013a), Ozone and organic nitrates over the eastern United States: Sensitivity to isoprene chemistry, *J. Geophys. Res. Atmos.*, *118*, 11,256–11,268, doi:10.1002/jgrd.50817.
- Mao, J., S. Fan, D. J. Jacob, and K. R. Travis (2013b), Radical loss in the atmosphere from Cu-Fe redox coupling in aerosols, *Atmos. Chem. Phys.*, *13*(2), 509–519, doi:10.5194/acp-13-509-2013.
- Mauldin III, R. L., et al. (2003), Highlights of OH, H<sub>2</sub>SO<sub>4</sub>, and methane sulfonic acid measurements made aboard the NASA P-3B during Transport and Chemical Evolution over the Pacific, *J. Geophys. Res.*, *108*(D20), 8796, doi:10.1029/2003JD003410.
- Meinshausen, M., et al. (2011), The RCP greenhouse gas concentrations and their extensions from 1765 to 2300, *Clim. Change*, *109*(1–2), 213–241, doi:10.1007/s10584-011-0156-z.
- Milliet, D. B., et al. (2010), Global atmospheric budget of acetaldehyde: 3-D model analysis and constraints from in-situ and satellite observations, *Atmos. Chem. Phys.*, *10*(7), 3405–3425, doi:10.5194/acp-10-3405-2010.
- Monks, S. A., et al. (2015), Multi-model study of chemical and physical controls on transport of anthropogenic and biomass burning pollution to the Arctic, *Atmos. Chem. Phys.*, *15*(6), 3575–3603, doi:10.5194/acp-15-3575-2015.
- Montzka, S. A., M. Krol, E. Dlugokencky, B. Hall, P. Jockel, and J. Lelieveld (2011), Small interannual variability of global atmospheric hydroxyl, *Science*, *331*(6013), 67–69, doi:10.1126/science.1197640.
- Murray, L. T., J. A. Logan, and D. J. Jacob (2013), Interannual variability in tropical tropospheric ozone and OH: The role of lightning, *J. Geophys. Res. Atmos.*, *118*, 11,468–11,480, doi:10.1002/jgrd.50857.

- Naik, V., et al. (2013), Preindustrial to present-day changes in tropospheric hydroxyl radical and methane lifetime from the Atmospheric Chemistry and Climate Model Intercomparison Project (ACCMIP), *Atmos. Chem. Phys.*, *13*(10), 5277–5298, doi:10.5194/acp-13-5277-2013.
- Navarro, M. A., et al. (2015), Airborne measurements of organic bromine compounds in the Pacific tropical tropopause layer, *Proc. Natl. Acad. Sci. U.S.A.*, *112*(45), 13,789–13,793, doi:10.1073/pnas.1511463112.
- Newell, R. E., and S. Gould-Stewart (1981), A stratospheric fountain?, *J. Atmos. Sci.*, *38*(12), 2789–2796, doi:10.1175/1520-0469(1981)038<2789:asf>2.0.co;2.
- Newton, R., G. Vaughan, H. M. A. Ricketts, L. L. Pan, A. J. Weinheimer, and C. Chemel (2016), Ozone profiles from the West Pacific Warm Pool: Measurements and validation, *Atmos. Chem. Phys.*, *16*, 619–634, doi:10.5194/acp-16-619-2016.
- NOAA (2014), ATom selected for funding under the NASA EVS-2 program, NOAA Earth Syst. Res. Lab. News and Events. [Available at [http://www.esrl.noaa.gov/csd/news/2014/160\\_1125.html](http://www.esrl.noaa.gov/csd/news/2014/160_1125.html)]
- Olson, J. R., et al. (2001), Seasonal differences in the photochemistry of the South Pacific: A comparison of observations and model results from PEM-Tropics A and B, *J. Geophys. Res.*, *106*, 32,749–32,766, doi:10.1029/2001JD900077.
- Olson, J. R., et al. (2004), Testing fast photochemical theory during TRACE-P based on measurements of OH, HO<sub>2</sub>, and CH<sub>2</sub>O, *J. Geophys. Res.*, *109*, D15510, doi:10.1029/2003JD004278.
- Palancar, G. G., R. E. Shetter, S. R. Hall, B. M. Toselli, and S. Madronich (2011), Ultraviolet actinic flux in clear and cloudy atmospheres: Model calculations and aircraft-based measurements, *Atmos. Chem. Phys.*, *11*(11), 5457–5469, doi:10.5194/acp-11-5457-2011.
- Pan, L. L., et al. (2015), Bimodal distribution of free tropospheric ozone over the tropical western Pacific revealed by airborne observations, *Geophys. Res. Lett.*, *42*, 7844–7851, doi:10.1002/2015GL065562.
- Pan, L. L., et al. (2016), The CONvective TRansport of Active Species in the Tropics (CONTRAST) Experiment, *Bull. Am. Meteorol. Soc.*, doi:10.1175/BAMS-D-14-00272.1.
- Prather, M. J., C. D. Holmes, and J. Hsu (2012), Reactive greenhouse gas scenarios: Systematic exploration of uncertainties and the role of atmospheric chemistry, *Geophys. Res. Lett.*, *39*, L09803, doi:10.1029/2012GL051440.
- Prinn, R. G., et al. (2005), Evidence for variability of atmospheric hydroxyl radicals over the past quarter century, *Geophys. Res. Lett.*, *32*, L07809, doi:10.1029/2004GL022228.
- Read, K. A., L. J. Carpenter, S. R. Arnold, R. Beale, P. D. Nightingale, J. R. Hopkins, A. C. Lewis, J. D. Lee, L. Mendes, and S. J. Pickering (2012), Multiannual observations of acetone, methanol, and acetaldehyde in remote tropical Atlantic air: Implications for atmospheric OVOC budgets and oxidative capacity, *Environ. Sci. Technol.*, *46*, 11,028–11,039, doi:10.1021/es302082p.
- Rex, M., et al. (2014), A tropical West Pacific OH minimum and implications for stratospheric composition, *Atmos. Chem. Phys.*, *14*(9), 4827–4841, doi:10.5194/acp-14-4827-2014.
- Ridder, T., C. Gerbig, J. Notholt, M. Rex, O. Schrems, T. Warneke, and L. Zhang (2012), Ship-borne FTIR measurements of CO and O<sub>3</sub> in the Western Pacific from 43° N to 35° S: An evaluation of the sources, *Atmos. Chem. Phys.*, *12*, 815–828, doi:10.5194/acp-12-815-2012.
- Ridley, B. A., and F. E. Grahek (1990), A small, low flow, high-sensitivity reaction vessel for NO chemiluminescence detectors, *J. Atmos. Oceanic Technol.*, *7*(2), 307–311, doi:10.1175/1520-0426(1990)007<0307:aslfhs>2.0.co;2.
- Saiz-Lopez, A., R. P. Fernandez, C. Ordóñez, D. E. Kinnison, J. C. Gómez Martín, J.-F. Lamarque, and S. Tilmes (2014), Iodine chemistry in the troposphere and its effect on ozone, *Atmos. Chem. Phys.*, *14*, 13,119–13,143, doi:10.5194/acp-14-13119-2014.
- Salawitch, R. J., D. K. Weisenstein, L. J. Kovalenko, C. E. Sioris, P. O. Wennberg, K. Chance, M. K. W. Ko, and C. A. McLinden (2005), Sensitivity of ozone to bromine in the lower stratosphere, *Geophys. Res. Lett.*, *32*, L05811, doi:10.1029/2004GL021504.
- Sander, S. P., et al. (2011), Chemical kinetics and photochemical data for use in atmospheric studies, Evaluation No. 17, Rep., Jet Propul. Lab., Pasadena, Calif.
- Saunders, S. M., M. E. Jenkin, R. G. Derwent, and M. J. Pilling (2003), Protocol for the development of the Master Chemical Mechanism, MCM v3 (Part A): Tropospheric degradation of non-aromatic volatile organic compounds, *Atmos. Chem. Phys.*, *3*(1), 161–180, doi:10.5194/acp-3-161-2003.
- Shetter, R. E., and M. Muller (1999), Photolysis frequency measurements using actinic flux spectroradiometry during the PEM-Tropics mission: Instrumentation description and some results, *J. Geophys. Res.*, *104*, 5647–5661, doi:10.1029/98JD01381.
- Shindell, D. T., et al. (2006), Multimodel simulations of carbon monoxide: Comparison with observations and projected near-future changes, *J. Geophys. Res.*, *111*, D19306, doi:10.1029/2006JD007100.
- Singh, H. B. (1977), Atmospheric halocarbons: Evidence in favor of reduced average hydroxyl radical concentration in troposphere, *Geophys. Res. Lett.*, *4*, 101–104, doi:10.1029/GL004i003p00101.
- Singh, H. B., and P. L. Hanst (1981), Peroxyacetyl Nitrate (PAN) in the unpolluted atmosphere: An important reservoir for nitrogen oxides, *Geophys. Res. Lett.*, *8*, 941–944, doi:10.1029/GL008i008p00941.
- Singh, H. B., A. Tabazadeh, M. J. Evans, B. D. Field, D. J. Jacob, G. Sachse, J. H. Crawford, R. Shetter, and W. H. Brune (2003), Oxygenated volatile organic chemicals in the oceans: Inferences and implications based on atmospheric observations and air-sea exchange models, *Geophys. Res. Lett.*, *30*(16), 1862, doi:10.1029/2003GL017933.
- Singh, H. B., et al. (2004), Analysis of the atmospheric distribution, sources, and sinks of oxygenated volatile organic chemicals based on measurements over the Pacific during TRACE-P, *J. Geophys. Res.*, *109*, D15507, doi:10.1029/2003JD003883.
- Stratospheric Processes and their Role in Climate (SPARC) (2013), SPARC Report on Lifetimes of Stratospheric Ozone-Depleting Substances, in *Their Replacements, and Related Species*, SPARC Rep. 6, WCRP-15/2013, edited by M. K. W. Ko et al. [Available at [www.sparc-climate.org/publications/sparc-reports/](http://www.sparc-climate.org/publications/sparc-reports/)]
- Spivakovsky, C. M., et al. (2000), Three-dimensional climatological distribution of tropospheric OH: Update and evaluation, *J. Geophys. Res.*, *105*, 8931–8980, doi:10.1029/1999JD901006.
- Stevenson, D. S., C. E. Johnson, W. J. Collins, R. G. Derwent, and J. M. Edwards (2000), Future estimates of tropospheric ozone radiative forcing and methane turnover—The impact of climate change, *Geophys. Res. Lett.*, *27*, 2073–2076, doi:10.1029/1999GL010887.
- Stevenson, D. S., et al. (2006), Multimodel ensemble simulations of present-day and near-future tropospheric ozone, *J. Geophys. Res.*, *111*, D08301, doi:10.1029/2005JD006338.
- Strahan, S. E., B. N. Duncan, and P. Hoor (2007), Observationally derived transport diagnostics for the lowermost stratosphere and their application to the GMI chemistry and transport model, *Atmos. Chem. Phys.*, *7*, 2435–2445, doi:10.5194/acp-7-2435-2007.
- Strode, S. A., B. N. Duncan, E. A. Yegorova, J. Kouatchou, J. R. Ziemke, and A. R. Douglass (2015), Implications of carbon monoxide bias for methane lifetime and atmospheric composition in chemistry climate models, *Atmos. Chem. Phys.*, *15*(20), 11,789–11,805, doi:10.5194/acp-15-11789-2015.
- Tan, D., et al. (2001), OH and HO<sub>2</sub> in the tropical Pacific: Results from PEM-Tropics B, *J. Geophys. Res.*, *106*, 32,667–32,681, doi:10.1029/2001JD900002.
- Tilmes, S., et al. (2015), Description and evaluation of tropospheric chemistry and aerosols in the Community Earth System Model (CESM1.2), *Geosci. Model Dev.*, *8*(5), 1395–1426, doi:10.5194/gmd-8-1395-2015.

- van Vuuren, D. P., et al. (2011), The representative concentration pathways: An overview, *Clim. Change*, 109(1–2), 5–31, doi:10.1007/s10584-011-0148-z.
- Voulgarakis, A., et al. (2013), Analysis of present day and future OH and methane lifetime in the ACCMIP simulations, *Atmos. Chem. Phys.*, 13(5), 2563–2587, doi:10.5194/acp-13-2563-2013.
- Wang, J. S., M. B. McElroy, J. A. Logan, P. I. Palmer, W. L. Chameides, Y. Wang, and I. A. Megretskaja (2008), A quantitative assessment of uncertainties affecting estimates of global mean OH derived from methyl chloroform observations, *J. Geophys. Res.*, 113, D12302, doi:10.1029/2007JD008496.
- Wennberg, P. O., S. Peacock, J. T. Randerson, and R. Bleck (2004), Recent changes in the air-sea gas exchange of methyl chloroform, *Geophys. Res. Lett.*, 31, L16112, doi:10.1029/2004GL020476.
- Wiedinmyer, C., S. K. Akagi, R. J. Yokelson, L. K. Emmons, J. A. Al-Saadi, J. J. Orlando, and A. J. Soja (2011), The Fire INventory from NCAR (FINN): A high resolution global model to estimate the emissions from open burning, *Geosci. Model Dev.*, 4(3), 625–641, doi:10.5194/gmd-4-625-2011.
- Williams, J. E., P. F. J. van Velthoven, and C. A. M. Brenninkmeijer (2013), Quantifying the uncertainty in simulating global tropospheric composition due to the variability in global emission estimates of Biogenic Volatile Organic Compounds, *Atmos. Chem. Phys.*, 13, 2857–2891, doi:10.5194/acp-13-2857-2013.
- World Meteorological Organization (2011), *Scientific Assessment of Ozone Depletion: 2010*, 516 pp., Global Ozone Res. and Monitoring Proj., Geneva, Switzerland.
- Wolfe, G. M., and J. A. Thornton (2011), The Chemistry of Atmosphere-Forest Exchange (CAFE) Model—Part 1: Model description and characterization, *Atmos. Chem. Phys.*, 11(1), 77–101, doi:10.5194/acp-11-77-2011.
- Wolter, K., and M. S. Timlin (2011), El Niño/Southern Oscillation behaviour since 1871 as diagnosed in an extended multivariate ENSO index (MEI.ext), *Int. J. Climatol.*, 31(7), 1074–1087, doi:10.1002/joc.2336.
- Zeng, G., and J. A. Pyle (2005), Influence of El Niño Southern Oscillation on stratosphere/troposphere exchange and the global tropospheric ozone budget, *Geophys. Res. Lett.*, 32, L01814, doi:10.1029/2004GL021353.
- Ziemke, J. R., S. Chandra, L. D. Oman, and P. K. Bhartia (2010), A new ENSO index derived from satellite measurements of column ozone, *Atmos. Chem. Phys.*, 10(8), 3711–3721, doi:10.5194/acp-10-3711-2010.
- Zondlo, M. A., M. E. Paige, S. M. Massick, and J. A. Silver (2010), Vertical cavity laser hygrometer for the National Science Foundation Gulfstream-V aircraft, *J. Geophys. Res.*, 115, D20309, doi:10.1029/2010JD014445.